

# Forward and adjoint simulations of seismic wave propagation on fully unstructured hexahedral meshes

Daniel Peter<sup>1</sup>, Dimitri Komatitsch<sup>2,3</sup>, Yang Luo<sup>1</sup>, Roland Martin<sup>2</sup>, Nicolas Le Goff<sup>2</sup>, Emanuele Casarotti<sup>4</sup>, Pieyre Le Loher<sup>2</sup>, Federica Magnoni<sup>4</sup>, Qinya Liu<sup>5</sup>, Céline Blitz<sup>2</sup>, Tarje Nissen-Meyer<sup>6</sup>, Piero Basini<sup>6</sup> and Jeroen Tromp<sup>1,7</sup>

<sup>1</sup> Princeton University, Department of Geosciences, 318 Guyot Hall, Princeton, NJ 08544, USA

<sup>2</sup> Université de Pau et des Pays de l'Adour, CNRS & INRIA Magique-3D, Laboratoire de Modélisation et d'Imagerie en Géosciences UMR 5212, Avenue de l'Université, 64013 Pau Cedex, France

<sup>3</sup> Institut universitaire de France, 103 boulevard Saint-Michel, 75005 Paris, France

<sup>4</sup> Istituto Nazionale di Geofisica e Vulcanologia, Via di Vigna Murata 605, 00143, Rome, Italy

<sup>5</sup> Department of Physics, University of Toronto, Ontario, Canada

<sup>6</sup> Institute of Geophysics, ETH Zurich, Sonneggstr. 5, CH-8092 Zurich, Switzerland

<sup>7</sup> Princeton University, Program in Applied & Computational Mathematics, Princeton, NJ 08544, USA

*Email:* [dpeter@princeton.edu](mailto:dpeter@princeton.edu)

January 2011

**Key words:** Computational seismology, Tomography, Interferometry, Wave propagation

## SUMMARY

We present forward and adjoint spectral-element simulations of coupled acoustic and (an)elastic seismic wave propagation on fully unstructured hexahedral meshes. Simulations benefit from recent advances in hexahedral meshing, load balancing and software optimization. Meshing may be accomplished using a mesh generation tool kit such as [CUBIT](#), and load balancing is facilitated by graph partitioning based on the [SCOTCH](#) library. Coupling between fluid and solid regions is incorporated in straightforward fashion using domain decomposition. Topography, bathymetry and Moho undulations may be readily included in the mesh, and physical dispersion and attenuation associated with anelasticity are accounted for using a series of standard linear solids. Finite-frequency Fréchet derivatives are calculated using adjoint methods in both fluid and solid domains. The software is benchmarked for a layer-cake model. We present various examples of fully unstructured meshes, snapshots of wavefields and finite-frequency kernels generated by Version 2.0 ‘Sesame’ of our widely used open source spectral-element package [SPECFEM3D](#).

## 1 INTRODUCTION

We present a new software package, [SPECFEM3D](#) Version 2.0 ‘Sesame’, capable of simulating forward and adjoint seismic wave propagation on fully unstructured hexahedral meshes of arbitrary shaped model domains. In view of unrelenting growth in computational power, it has become more-and-more important to develop software capable of harnessing powerful computers to address a broad range of seismological forward and inverse problems. A well-established numerical technique for solving such problems in a fast and highly accurate manner is the spectral-element method (SEM). The SEM was originally developed in computational fluid dynamics (Patera 1984; Maday & Patera 1989) and has been successfully adapted to address problems in seismic wave propagation. Early seismic wave propagation applications of the SEM, utilizing Legendre basis functions and a perfectly diagonal mass matrix, include Cohen et al. (1993), Komatitsch (1997), Faccioli et al. (1997), Casadei & Gabellini (1997), Komatitsch & Vilotte (1998) and Komatitsch & Tromp (1999), whereas applications involving Chebyshev basis func-

tions and a nondiagonal mass matrix include Seriani & Priolo (1994), Priolo et al. (1994) and Seriani et al. (1995).

The SEM is a continuous Galerkin technique, which may be made discontinuous (Bernardi et al. 1994; Chaljub 2000; Kopriva et al. 2002; Chaljub et al. 2003; Legay et al. 2005; Kopriva 2006; Wilcox et al. 2010; Acosta Minolia & Kopriva 2011); it is then close to a particular case of the discontinuous Galerkin technique (Reed & Hill 1973; Arnold 1982; Falk & Richter 1999; Hu et al. 1999; Cockburn et al. 2000; Giraldo et al. 2002; Rivière & Wheeler 2003; Monk & Richter 2005; Grote et al. 2006; Ainsworth et al. 2006; Bernacki et al. 2006; Dumbser & Käser 2006; De Basabe et al. 2008; de la Puente et al. 2009; Wilcox et al. 2010; De Basabe & Sen 2010; Étienne et al. 2010), with optimized efficiency because of its tensorized basis functions (Wilcox et al. 2010; Acosta Minolia & Kopriva 2011).

An important feature of the SEM is that it can accurately handle very distorted mesh elements (Oliveira & Seriani 2011), and thus conforming non-structured mesh doubling bricks can efficiently accommodate mesh size variations (Komatitsch & Tromp 2002a; Komatitsch et al. 2004; Lee et al. 2008, 2009a,b). The method has very good accuracy and convergence properties, such as a spectral rate of convergence (Canuto et al. 1988; Maday & Patera 1989; Seriani & Priolo 1994; Deville et al. 2002; Cohen 2002; De Basabe & Sen 2007; Seriani & Oliveira 2008). In this sense the SEM is close to the family of pseudo-spectral methods (see e.g., Canuto et al. 1988; Carcione et al. 1988a, 1992; Carcione & Wang 1993; Komatitsch et al. 1996), but combined with the flexibility of finite elements, in particular in terms of mesh design. For reviews of the SEM in seismology, see e.g., Komatitsch et al. (2005), Chaljub et al. (2007), Tromp et al. (2008) and Fichtner (2010). The SEM is well suited to parallel implementations on very large supercomputers (Komatitsch & Tromp 2002a; Komatitsch et al. 2003; Tsuboi et al. 2003; Komatitsch et al. 2008; Carrington et al. 2008; Komatitsch et al. 2010b) as well as on clusters of GPU accelerating graphics cards (Komatitsch et al. 2009, 2010a; Komatitsch 2011). Tensor products inside each element may be optimized to reach very high efficiency (Deville et al. 2002), and mesh point and element numbering may be optimized to reduce processor cache misses and improve cache reuse (Komatitsch et al. 2008). The SEM can

handle triangular (in 2D) or tetrahedral (in 3D) elements (Wingate & Boyd 1996; Taylor & Wingate 2000; Komatitsch et al. 2001; Cohen 2002; Mercerat et al. 2006), as well as mixed meshes, although with increased cost and reduced accuracy in these non-tensorized elements, as in the discontinuous Galerkin method.

In many cases of practical seismological interest, using a conforming mesh and a continuous formulation is sufficient, because in most geological models material property contrasts are not too dramatic. When this ceases to be true, requiring a discontinuous formulation, one can either turn to a discontinuous version of the SEM (Bernardi et al. 1994; Chaljub 2000; Kopriva et al. 2002; Chaljub et al. 2003; Legay et al. 2005; Kopriva 2006; Wilcox et al. 2010; Acosta Minolia & Kopriva 2011) or to a discontinuous Galerkin technique. A discontinuous formulation is particularly suitable for dynamic rupture simulations, because high frequencies or supershear rupture need to be accommodated near the fault, where a significantly denser mesh and a more sophisticated (upwind) time scheme are required, thereby suppressing the amplification of unstable modes (see e.g., Benjemaa et al. 2007; de la Puente et al. 2009; Benjemaa et al. 2009; Tago et al. 2010). Another example that may require a discontinuous formulation involves the resolution of a shallow geotechnical layer, in which seismic shear wavespeeds may be reduced by an order of magnitude.

For seismological applications, the SEM has been successfully implemented for three-dimensional global- and regional-scale simulations (Komatitsch & Vilotte 1998; Paolucci et al. 1999; Chaljub 2000; Komatitsch & Tromp 2002a,b; Capdeville et al. 2003; Chaljub & Valette 2004; Fichtner et al. 2009a), as well as local-scale simulations in complex and/or densely populated regions, for example in southern California, USA (Komatitsch et al. 2004; Tape et al. 2009, 2010), Taipei, Taiwan (Lee et al. 2008, 2009a,b), Caracas, Venezuela (Delavaud et al. 2006) and Grenoble, France (Chaljub et al. 2005; Stupazzini et al. 2009; Chaljub et al. 2010). The SEM may also be used to study elastic wave propagation on smaller scales, for instance the propagation of ultrasonic waves in crystals (van Wijk et al. 2004).

Two complementary SEM software packages—namely, [SPECFEM3D\\_GLOBE](#) for global and regional simulations, and [SPECFEM3D](#) for local simulations—are feature-rich, well

benchmarked and documented implementations. Data parallelism in the SEM is efficiently exploited using the Message-Passing Interface (MPI) standard, crucial for modern high-performance computing. These open source packages are freely available via the Computational Infrastructure for Geodynamics ([CIG](#)) and widely used by the seismological community.

To extend the range of local-scale applications, easing the task of mesh generation is paramount. The two community software packages separate a simulation into two distinct steps: first, creation of a hexahedral mesh, and second, solution of the seismic wave equation. This separation avoids the overhead of remeshing when running multiple simulations for the same region, e.g., repeated simulations at the same resolution. Focussing on local-scale simulations, previous versions of [SPECFEM3D](#) used an internal mesher which was explicitly tied to the specific purposes of the package: all geological models were based on a layercake model. Consequently, the solver was restricted by its internal mesher. It was impossible to run spectral-element simulations on more complex 3D models without significant recoding, nor was it possible to run such simulations in regions of interest for on- and off-shore exploration seismology, because acoustic wave propagation in fluids was not supported by the package.

The purpose of this article is to present forward and adjoint simulations in various 3D models using the new software package, [SPECFEM3D](#) Version 2.0 ‘Sesame’, thereby illustrating its current capabilities. The original [SPECFEM3D](#) package for local simulations was extended, improved and optimized in various ways. The Version 2.0 ‘Sesame’ release includes a more flexible internal mesher and accommodates more powerful external meshers, such as [CUBIT](#) (Blacker et al. 1994; White et al. 1995; Mitchell 1996; Casarotti et al. 2008). Adding such external meshers into the workflow greatly increases flexibility for high-performance applications, as illustrated by the [GeoELSE](#) software package (Casadei & Gabellini 1997; Stupazzini et al. 2009; Chaljub et al. 2010). Advantages of [GeoELSE](#) include the accommodation of visco-plastic and non-linear rheologies, whereas benefits of [SPECFEM3D](#) include coupled fluid-solid domains and adjoint capabilities; the latter enable one to address seismological inverse problems. Load balancing parallel simulations in [SPECFEM3D](#) is accomplished based on the graph partitioning software

package **SCOTCH** (Pellegrini & Roman 1996; Chevalier & Pellegrini 2008). The new package facilitates coupled forward and adjoint acoustic/(an)elastic simulations, which are especially interesting for problems in exploration seismology, ocean acoustics and medical tomography. The new software is freely available under the GNU GPL Version 2 license via [CIG](#).

## 2 GOVERNING EQUATIONS

Let us briefly summarize the equations governing seismic wave propagation implemented in **SPECFEM3D**. For more technical details, the reader is referred to Komatitsch & Tromp (1999). **SPECFEM3D** Version 2.0 ‘Sesame’ implements wave propagation in coupled (an)elastic and acoustic materials on local scales. We may thus safely neglect additional effects that would arise from self-gravitation and rotation (Komatitsch & Tromp 2002b; Komatitsch et al. 2005; Chaljub et al. 2007), which are important at longer periods. In the following, we first discuss (an)elastic wave propagation and subsequently consider acoustic waves.

### 2.1 Elastic domain

For elastic materials, the displacement wavefield  $\mathbf{s}(\mathbf{x}, t)$  is governed by

$$\rho \partial_t^2 \mathbf{s} = \nabla \cdot \mathbf{T} + \mathbf{f}, \quad (1)$$

where  $\rho$  denotes mass density,  $\mathbf{T}$  the stress tensor and  $\mathbf{f}$  the seismic source. On free surfaces, the traction vector must vanish, i.e.,

$$\hat{\mathbf{n}} \cdot \mathbf{T} = \mathbf{0}, \quad (2)$$

where  $\hat{\mathbf{n}}$  denotes the unit outward normal on the surface. On boundaries between different elastic materials, both traction  $\hat{\mathbf{n}} \cdot \mathbf{T}$  and displacement  $\mathbf{s}$  need to be continuous. On boundaries between elastic and acoustic domains, traction  $\hat{\mathbf{n}} \cdot \mathbf{T}$  and the normal component of displacement  $\hat{\mathbf{n}} \cdot \mathbf{s}$  need to be continuous. The initial conditions are

$$\mathbf{s}(\mathbf{x}, 0) = \mathbf{0}, \quad \partial_t \mathbf{s}(\mathbf{x}, 0) = \mathbf{0}. \quad (3)$$

We thus initiate the simulation in a medium at rest. To accommodate simulations under pre-stressed conditions, these initial conditions may be modified in an appropriate manner.

For elastic materials, the force  $\mathbf{f}$  in eq. (1) represents the earthquake, which for a simple point source may be written as

$$\mathbf{f} = -\mathbf{M} \cdot \nabla \delta(\mathbf{x} - \mathbf{x}_s) S(t), \quad (4)$$

where  $\mathbf{M}$  denotes the moment tensor,  $\mathbf{x}_s$  the source location,  $\delta(\mathbf{x} - \mathbf{x}_s)$  the Dirac delta distribution located at  $\mathbf{x}_s$  and  $S(t)$  the source-time function. The software also accommodates kinematic rupture simulations, which may be captured by prescribing a moment-density tensor field.

The stress tensor  $\mathbf{T}$  is linearly related to the strain via the constitutive relationship

$$\mathbf{T} = \mathbf{c} : \nabla \mathbf{s}, \quad (5)$$

where  $\mathbf{c}$  denotes the stiffness tensor that describes the elastic properties of the medium. The implementation is general and can handle a fully anisotropic tensor with 21 independent parameters (Chen & Tromp 2007; Sieminski et al. 2007a,b). Using a linear constitutive relationship is valid under the assumption that perturbations to the reference state are small. Note that nonlinear effects are sometimes observed, e.g., nonlinear soil amplification, and nonlinear constitutive relationships become important for studying such effects, e.g., for risk mitigation (Xu et al. 2003; Dupros et al. 2010).

In an anelastic medium, we approximate an absorption-band solid using a series of  $L$  standard linear solids (Liu et al. 1976), and model the time evolution of the isotropic shear modulus  $\mu$  by

$$\mu(t) = \mu_R \left[ 1 - \sum_{l=1}^L \left( 1 - \frac{\tau_l^\epsilon}{\tau_l^\sigma} \right) e^{-t/\tau_l^\sigma} \right] H(t), \quad (6)$$

where  $\mu_R$  denotes the relaxed modulus,  $H(t)$  the Heaviside function and  $\tau_l^\sigma$  &  $\tau_l^\epsilon$  the stress and strain relaxation times of the  $l$ th standard linear solid. Experience shows that three solids generally suffice for simulating an absorption band (Emmerich & Korn 1987). For further details, see Carcione et al. (1988b), Robertsson (1996), Day & Bradley (2001), Moczo & Kristek (2005), Komatitsch et al. (2005), Carcione (2007) and Savage

et al. (2010). Simulations of seismic wave propagation in laboratory-scale rock samples or in the context of medical tomography involve very high frequencies (in the kHz or even MHz range), and strong attenuation must be taken into account.

The SEM solves the equations of motion in the weak form, which is obtained by dotting the momentum equation (1) with an arbitrary test vector  $\mathbf{w}$  and integrating by parts over the model volume  $\Omega$ . We focus on elastic domains and consider coupling interfaces with acoustic domains. Thus, we obtain

$$\int_{\Omega} \rho \mathbf{w} \cdot \partial_t^2 \mathbf{s} d^3x = \int_{\partial\Omega} \hat{\mathbf{n}} \cdot \mathbf{T} \cdot \mathbf{w} d^2x - \int_{\Omega} \nabla \mathbf{w} : \mathbf{T} d^3x + \mathbf{M} : \nabla \mathbf{w}(\mathbf{x}_s) S(t). \quad (7)$$

Note that in this formulation the traction-free surface condition is implicitly accounted for by setting the contribution from the free surface to zero.

When and where necessary, we use Clayton-Engquist-Stacey absorbing conditions (Clayton & Engquist 1977; Stacey 1988; Quarteroni et al. 1998) to absorb outgoing waves on fictitious boundaries of the mesh, thereby representing a semi-infinite domain. It would be more efficient to use a Perfectly Matched Layer (PML) (see e.g., Komatitsch & Martin 2007; Martin et al. 2008c; Martin & Komatitsch 2009), but a parallel implementation with good load-balancing properties is challenging because additional equations need to be solved. This issue becomes important when high-order time marching is required to reduce numerical dispersion in difficult case studies that involve complex media with poroelastic or viscoelastic rheologies (Martin et al. 2008b, 2010) or Newtonian compressible fluids (Martin & Couder-Castaneda 2010). Consequently, additional computations need to be performed in PML layers, in particular in corners, where contributions along several directions are summed (Komatitsch & Martin 2007).

At a solid-fluid boundary, the interface integral over the coupling surface  $\partial\Omega$  is used to exchange pressure from the fluid  $p_{\text{fluid}}$  to the solid:  $\hat{\mathbf{n}} \cdot \mathbf{T} = -p_{\text{fluid}} \hat{\mathbf{n}}$ .

## 2.2 Acoustic domain

We define a scalar potential  $\phi$  such that the displacement  $\mathbf{s}$  may be written as

$$\mathbf{s} = \rho^{-1} \nabla \phi. \quad (8)$$

The equation of motion in terms of the potential  $\phi$  becomes

$$\kappa^{-1} \partial_t^2 \phi = \nabla \cdot (\rho^{-1} \nabla \phi) + f, \quad (9)$$

where  $\kappa$  denotes the bulk modulus. It follows that velocity  $\mathbf{v}$  and pressure  $p$  may be expressed as:

$$\mathbf{v} = \rho^{-1} \nabla \partial_t \phi, \quad (10)$$

$$p = -\kappa (\nabla \cdot \mathbf{s}) = -\partial_t^2 \phi. \quad (11)$$

The resulting formulation for pressure  $p$  is the reason why we choose to define the potential  $\phi$  as in equation (8). Since pressure is continuous across first-order discontinuities, it follows that  $\partial_t^2 \phi$  and thus  $\phi$  must be continuous, a requirement which is honored automatically by the basis functions of the SEM. The source  $f$  may be expressed in terms of pressure  $P$  acting at location  $\mathbf{x}_s$ :

$$f = -\kappa^{-1} P(t) \delta(\mathbf{x} - \mathbf{x}_s). \quad (12)$$

Note that the source is multiplied by a factor  $\kappa^{-1}$  due to the formulation used in eq. (9).

Using Gauss’ theorem and a scalar test function  $w$ , the weak form becomes

$$\int_{\Omega} \kappa^{-1} w \partial_t^2 \phi d^3 \mathbf{x} = \int_{\partial\Omega} \rho^{-1} w \hat{\mathbf{n}} \cdot \nabla \phi d^2 \mathbf{x} - \int_{\Omega} \rho^{-1} \nabla w \cdot \nabla \phi d^3 \mathbf{x} - \kappa^{-1} P(t) w(\mathbf{x}_s). \quad (13)$$

At the free surface  $\partial\Omega$  we set the pressure  $p = -\partial_t^2 \phi = 0$ , thereby enforcing  $\phi = 0$ ,  $\partial_t \phi = 0$  and  $\partial_t^2 \phi = 0$ , i.e., we implement a Dirichlet boundary condition along the surface. At a fluid-solid boundary, the interface coupling integral may be used to exchange the normal component of displacement between fluid and solid:  $\rho^{-1} \hat{\mathbf{n}} \cdot \nabla \phi = \hat{\mathbf{n}} \cdot \mathbf{s}_{\text{solid}}$ .

### 3 MESHING, MESH PARTITIONING AND LOAD BALANCING

The first step in a SEM consists of constructing a high-quality mesh for the region of interest. In this section, we outline the key issues based on various 3D examples. Fig. 1 draws the schematic workflow from meshing and partitioning to finally running spectral-element simulations. We discuss each phase separately, focussing on the use of an external mesher, in our case **CUBIT** (Blacker et al. 1994).

### 3.1 Hexahedral meshing

We subdivide the model volume  $\Omega$  into a set of non-overlapping, hexahedral elements. We impose that the discretization creates a conforming mesh, i.e., elements match on a full face or edge, and the mesh cannot be discontinuous. Using the SEM with hexahedral elements leads to computational benefits over tetrahedral finite elements (Komatitsch et al. 2001; Mercerat et al. 2006; Vos et al. 2010). Especially for parallel implementations, taking advantage of the diagonal mass matrix and optimized tensor products is critical in terms of computational speed (Komatitsch et al. 2003; Carrington et al. 2008; Vos et al. 2010). Hexahedral meshing is also attractive for the SEM because it benefits from reduced errors and generally smaller element counts compared to tetrahedral meshing (Hesthaven & Teng 2000; Komatitsch et al. 2001; Vos et al. 2010).

Unfortunately, automatic 3D hexahedral mesh generation is more demanding than unstructured tetrahedral meshing (Shepherd & Johnson 2008; Staten et al. 2010). In order to construct hexahedral meshes, our examples make use of an external hexahedral mesher, such as **CUBIT** (Blacker et al. 1994). We focus on this particular mesh generation tool kit because it is a well documented and feature-rich package, on which most of our own experience is based. One may readily use other meshing tools, such as **Abaqus** (SIMULIA 2008), **ANSYS** (ANSYS 2011), **GOCAD** (Mallet 1992; Caumon et al. 2009), **GiD** (Gardia-Donoro et al. 2010; Ribó et al. 2011), **Gmsh** (Geuzaine & Remacle 2009), **TrueGrid** (Rainsberger 2006; Noble & Nuss 2004) or **Salome** (Ribes & Caremoli 2007; Bergeaud et al. 2010).

Fig. 2 shows several examples of fully unstructured hexahedral meshes. In the Mount St. Helens region, the mesh employs a mesh tripling layer to increase resolution at the topographic surface. Tripling is the default refinement in **CUBIT** for subdividing hexahedral elements in a conforming fashion. Surface topography is imported using Shuttle Radar Topographic Mission (**SRTM**) data, converted to Universal Transverse Mercator (UTM) coordinates with an original resolution of 90 m (Jarvis et al. 2008). Meshing is performed automatically by **CUBIT** using a sweep algorithm. The resolution of the mesh enables seismic wave simulations with frequencies up to  $\sim$ 1.5 Hz. The Mesh for the L’Aquila region, Italy, consists of  $\sim$ 7 M hexahedra with an element size of  $\sim$ 90 m

at the top surface. This mesh facilitates simulations of seismic wave propagation up to  $\sim 5$  Hz. For the exploration geophysics model, the hexahedral mesh honors a salt dome body inside a 3D model capped by a water layer. The Mesh for asteroid 433-Eros with a close-bound surface has a resolution of roughly 300 m. Finally, the filled coffee cup model discretized into hexahedra couples an elastic domain for the cup with an acoustic domain for the coffee inside the cup.

In order to ensure compatibility with previous versions of **SPECFEM3D** (see e.g., Komatitsch et al. 2004; Liu et al. 2004), the in-house mesher based on analytical linear interpolation from the top to the bottom of the mesh has been adapted to the new code structure. It facilitates the design of simpler, alternative meshes for layercake models.

### 3.2 Partitioning and load balancing

Balancing the computational load and distributing the mesh on a large number of cores is crucial for optimized high-performance simulations (Martin et al. 2008a). In order to do so, we make use of an external partitioner, namely **SCOTCH** (Pellegrini & Roman 1996; Chevalier & Pellegrini 2008), which we use to balance spectral-element computations on an arbitrary number of cores. An alternative partitioner able to fulfill these tasks is **METIS** (Karypis & Kumar 1998), but **SCOTCH** is more actively maintained (Chevalier & Pellegrini 2008) and performs better in many cases that we have tested.

Especially for simulations involving coupled elastic and acoustic domains, balancing the mesh becomes paramount. Most of the computation time is spent resolving the divergence of the stress tensor in each element. The computational cost for an elastic element is approximately four times larger than for an acoustic element, which may be established by running simulations for one domain at a time. During partitioning, we therefore weight each element according to its associated domain type and computational cost to balance the overall numerical cost rather than simply the number of elements between partitions. The major improvement in **SPECFEM3D** code performance focuses on these tensor products, using highly efficient algorithms developed by Deville et al. (2002) and optimizing cache usage. Another key aspect of mesh partitioning is minimization of the number of edge cuts, because this reduces the amount of MPI communications between

processor cores (an edge cut occurs when two contiguous elements are assigned to distinct cores). On machines comprising a very large number of cores, it is crucial to resort to non-blocking communications between compute nodes, for instance using non-blocking MPI message passing, in order to obtain good performance scaling (Danielson & Namburu 1998; Martin et al. 2008a; Komatitsch et al. 2008).

Fig. 3 presents a simple example of partitioning and load balancing the mesh around Mount St. Helens, as shown in Fig. 2. For illustrative purposes, we decompose the mesh onto four cores using the **SCOTCH** library. The total number of spectral-elements is  $\sim 24,000$ , such that each partition contains  $\sim 6,000$  elements after decomposition. Partitioning and load balancing equally distributes the elements over the different cores, since the whole domain is purely elastic. A partitioner such as **SCOTCH** can also load balance computationally more complex meshes, for example containing PML elements along absorbing boundaries of the model; this is the subject of future research.

In a final, separate step we generate mesh databases for each partition needed for the spectral-element solver. These databases contain Gauss-Lobatto-Legendre (GLL) points for all spectral elements. Material properties are assigned to these GLL points, and thus sampling resolution of a geological model not only depends on element size but also on polynomial degree. Furthermore, the generation of mesh databases automatically detects interfaces between elastic and acoustic domains, needed for coupling seismic waves from one domain to another. Load-balancing of the simulation persists, because we keep the polynomial degree fixed for all spectral elements. Note that this final step of generating mesh databases provides additional freedom in assigning and changing wavespeeds, which is important for seismic inversion procedures.

### 3.3 Overlapping computation and communication

The elements that compose the mesh slices shown in Figures 2 and 3 are in contact through a common face, edge or point. To allow for overlap of communication between compute nodes with computations within each mesh slice —thereby speeding up the simulation—a list of all elements in contact with any other mesh slice through a common

face, edge or point is created. Members of this list are termed ‘outer’ elements, and all other elements are termed ‘inner’ elements, as illustrated in Figure 4.

Once the outer elements have been identified following a standard procedure (see e.g., Danielson & Namburu 1998; Martin et al. 2008a; Micikevicius 2009; Michéa & Komatitsch 2010; Komatitsch et al. 2010a; Komatitsch 2011), MPI buffers are filled and a non-blocking MPI call is issued, which initiates communication and returns immediately. While MPI messages are traveling across the network, computations are performed on inner elements. Achieving effective overlap requires that the ratio of the number of inner to outer elements is sufficiently large, a condition which is satisfied for suitably large mesh slices. Under these circumstances, MPI data transfer will generally finish before the completion of computations on inner elements.

## 4 SAMPLE SIMULATIONS

In this section, we present various simulations with increasing complexity to highlight the flexibility of our new spectral-element package. We start with a layercake model and finish with an example of an arbitrarily-shaped model.

### 4.1 Validation example: Two-Layer model

The SEM has been well benchmarked against discrete wavenumber methods for layercake models by Komatitsch & Tromp (1999). Here we compare their two-layer model solution (Figure 8, left) against the solution obtained by the new code. The model has a horizontal size of  $134 \text{ km} \times 134 \text{ km}$ , with a depth of 60 km. We discretize the model into 70,200 elements, using an approximate element size of 1,000 m at the top and 4,500 m at the bottom. A mesh tripling layer is placed below the upper layer, between 3 km and 10 km, with the wavespeed properties of the lower layer. We use [SCOTCH](#) to partition the model onto six cores, each with 11,700 elements. The final mesh is generated using GLL points for a polynomial degree  $N = 5$ , which results in 9,025,941 global mesh points.

A vertical force is placed at a depth of 25.05 km in the middle of the model. The source-time function is a Ricker wavelet with a dominant frequency of 0.4 Hz. The simulation uses a time step of 6.5 ms and propagates for 6,000 steps. We compare our solution

with seismograms obtained by Komatitsch & Tromp (1999) (Figure 9). The mesh and seismograms are shown in Fig. 5. The seismograms match very closely with the reference solutions, exhibiting almost identical displacements. Maximum waveform differences reach  $\sim 0.3\%$ , arising from differences in mesh geometry and source implementation.

The performance of the code is summarized in Fig. 6, using simulations with the optimized routines by Deville et al. (2002) and a polynomial degree  $N = 4$ . We are interested in how the code behaves when the number of calculations is decreased linearly with the number of CPU cores (strong scaling), and how performance varies when the number of calculations on each core is kept constant while increasing the total number of CPU cores (weak scaling). To assess strong scaling, we fix the total mesh size but vary the number of CPU cores used for the simulation. We run the simulation for a duration of 4,000 time steps and show the corresponding average elapsed time per time step in Fig. 6(a). More interesting for high-performance applications, we assess weak scaling by fixing the problem size per processor and varying the number of CPU cores. This leads to higher mesh resolutions for an increasing number of CPU cores but should keep the average elapsed time per time step constant. We summarize the simulation times in Fig. 6(b). The computations were performed on a high-performance cluster with compute nodes consisting of two Intel Nehalem quad-core processors; each core has 3 GB of RAM. The code scales linearly within  $\sim 90\%$  up to 256 CPU cores for both strong and weak scaling, achieving excellent performance on this parallel system. Note that for the strong scaling examples shown here, simulations using more than 64 CPUs see a performance decrease since communications no longer overlap, thus they no longer profit from the default non-blocking MPI scheme (Martin et al. 2008a).

## 4.2 Mount St. Helens example: Layercake model with surface topography

In order to include surface topography, we import [SRTM](#) data with an original resolution of 90 m (Jarvis et al. 2008) and convert it to UTM coordinates for the corresponding UTM zone. We read in this dataset using [CUBIT](#) and create a surface honoring these data points. A 3D volume is built manually with topography on top.

The simulation uses an explosive source at a depth of 5 km. In Fig. 7, we show the vertical

displacement field at the free surface at consecutive times. Note that once the wavefield hits the model boundary, it gets absorbed by the Clayton-Engquist-Stacey absorbing boundary conditions.

### 4.3 L’Aquila example: Layercake model honoring surface and Moho topography

The purpose of this example is to show that additional surfaces may be honored by the mesh, for example the Moho. We import not only surface topography, but also create a Moho surface that is honored by the boundaries of the spectral elements. The mesh for the L’Aquila region was built using an additional ‘Python’ library that semi-automates the mesh creation process with [CUBIT](#) (Casarotti et al. 2008). Once these mesh files are constructed, the default partitioning and database generation process may be used to create fully load-balanced spectral-element simulations on an arbitrary number of parallel processors.

Fig. 8 shows several snapshots of the seismic wavefield at consecutive times for an anelastic material, using a kinematic source description for the April 6, 2009, L’Aquila earthquake. Simulations are accurate up to 5 Hz and may be used to discriminate between different wavespeed models and/or kinematic source solutions. These high-frequency simulations may be used to assess the response of engineered structures and may guide the development of better seismic building codes for the L’Aquila region.

### 4.4 SEG/EAGE salt dome example: Exploration model

Our new spectral-element package can combine acoustic and (an)elastic simulations by coupling these distinct domains. In this example, we generate acoustic waves in the top water layer and propagate them down through a salt dome body included in the lower, anelastic domain. The mesh honors the surface of the salt dome and the fluid-solid boundary, i.e., the bathymetry.

Fig. 9 shows the acoustic wavefield at the free surface of the water layer at different times. The source is a pressure source, located slightly below the free surface in the water layer, with a Ricker source-time function. The wavefield is reflected and refracted by the salt

dome in the anelastic domain below the water layer. Note how these reflected/refracted waves, which include P-to-S converted waves, are recorded in the water layer.

#### 4.5 Asteroid example: Arbitrarily-shaped model

This final example shows that our new software package may be used for simulating wave propagation in arbitrarily-shaped models, such as asteroid Eros, which was imaged by the NEAR spacecraft in 2000–2001. This silicated asteroid is 34 km long with a peanut-like shape and is thought to be covered with a regolith layer, corresponding to a blanket of loose material crushed by impacts (Richardson et al. 2005). We meshed the asteroid with 5,797,440 hexahedral elements having an approximate resolution of 70 m. To simulate a thin, 70 m regolith layer superimposed on strong bedrock, as suggested by Robinson et al. (2002), we assigned a low-wavespeed material to the elements touching the free surface and a high-wavespeed material to elements inside the asteroid, representing solid bedrock.

We simulated the propagation of seismic waves from a source represented by a point force normal to the surface. The source-time function corresponds to a Dirac pulse low-pass filtered up to a cutoff frequency of 5 Hz. Fig. 10 displays wavefield snapshots for the first  $\sim$ 10 seconds of the simulation. It shows the propagation of P, S and surface waves with a refocusing effect on the opposite side. The regolith layer strongly increases physical dispersion of surface waves. Peak ground accelerations are plotted in Fig. 11 for a simulation without a regolith layer, showing that refocussing occurs on the asteroid.

## 5 ADJOINT SENSITIVITY KERNELS

An important goal in seismology is to use differences between observed and simulated seismograms to improve Earth and source models, that is, we are interested in the inverse problem. An elegant way to address this issue is to take advantage of adjoint methods (Tarantola 1984; Tromp et al. 2005) to calculate Fréchet derivatives for a predefined objective function. These derivatives may then be used in a conjugate-gradient approach to minimize differences between data and synthetics. The key ingredients of such an adjoint approach are sensitivity kernels. Following Tromp et al. (2005), Liu & Tromp

(2006, 2008) and Tromp et al. (2010), we show examples of sensitivity kernels for various models using our new software package.

### 5.1 Elastic sensitivity kernels

Following Tromp et al. (2005), we may write the variation of a misfit function  $\chi$  as

$$\delta\chi = \int_V (K_\rho \delta \ln \rho + K_{c_{jklm}} \delta c_{jklm}) d^3\mathbf{x}, \quad (14)$$

where  $\delta \ln \rho = \delta \rho / \rho$  denotes relative perturbations in density and  $\delta c_{jklm}$  denotes perturbations in the elastic tensor. The misfit kernels are given by

$$K_\rho = -\rho \int_0^T \mathbf{s}^\dagger(T-t) \cdot \partial_t^2 \mathbf{s}(t) dt, \quad (15)$$

$$K_{c_{jklm}} = - \int_0^T \epsilon_{jk}^\dagger(T-t) \epsilon_{lm}(t) dt, \quad (16)$$

where  $\epsilon_{lm}$  and  $\epsilon_{jk}^\dagger$  denote elements of the strain and adjoint strain tensors, and where we have suppressed the spatial dependence to avoid clutter.

In an isotropic model, we have  $c_{jklm} = (\kappa - 2\mu/3) \delta_{jk} \delta_{lm} + \mu (\delta_{jl} \delta_{km} + \delta_{jm} \delta_{kl})$ , and thus eq. (14) may be rewritten as

$$\delta\chi = \int_V (K_\rho \delta \ln \rho + K_\mu \delta \ln \mu + K_\kappa \delta \ln \kappa) d^3\mathbf{x}. \quad (17)$$

The isotropic misfit kernels  $K_\mu$  and  $K_\kappa$  are defined by

$$K_\mu = -2\mu \int_0^T \mathbf{D}^\dagger(T-t) : \mathbf{D}(t) dt, \quad (18)$$

$$K_\kappa = -\kappa \int_0^T [\nabla \cdot \mathbf{s}^\dagger(T-t)] [\nabla \cdot \mathbf{s}(t)] dt, \quad (19)$$

where  $\mathbf{D} = \frac{1}{2}[\nabla \mathbf{s} + (\nabla \mathbf{s})^T] - \frac{1}{3}(\nabla \cdot \mathbf{s}) \mathbf{I}$  and  $\mathbf{D}^\dagger = \frac{1}{2}[\nabla \mathbf{s}^\dagger + (\nabla \mathbf{s}^\dagger)^T] - \frac{1}{3}(\nabla \cdot \mathbf{s}^\dagger) \mathbf{I}$  are the traceless strain deviator and its adjoint, respectively. In terms of a parameterization involving compressional wavespeed  $\alpha$ , shear wavespeed  $\beta$  and density  $\rho$ , the corresponding kernels are given by a linear combination of these primary kernels (Tromp et al. (2005), eq. 20):

$$K_\alpha = 2 \left( \frac{\kappa + \frac{4}{3}\mu}{\kappa} \right) K_\kappa, \quad K_\beta = 2 \left( K_\mu - \frac{4}{3} \frac{\mu}{\kappa} K_\kappa \right), \quad K'_\rho = K_\kappa + K_\mu + K_\rho. \quad (20)$$

Note that a suitable parameterization for isotropic inversions is to use bulk sound

wavespeed  $\Phi = \sqrt{\kappa/\rho}$ , shear wavespeed  $\beta$  and density  $\rho$  (Tarantola 1987). Bulk sound and shear wavespeeds are independent combinations of the bulk and shear moduli  $\kappa$  and  $\mu$ . The corresponding kernels are given by

$$K_\Phi = 2K_\kappa, \quad K'_\beta = 2K_\mu, \quad K'_\rho = K_\kappa + K_\mu + K_\rho. \quad (21)$$

We place an explosive source at a depth of 7 km and a horizontal distance of 16 km from the receiver in a homogeneous model with topography around Mount St. Helens. The P wave at the receiver is used to construct a travelttime adjoint source for the kernel simulation. Fig. 12(a) shows the isotropic kernels  $K_\kappa$ ,  $K_\mu$  and  $K_\rho$ , and Fig. 12(b) the isotropic kernels  $K_\alpha$ ,  $K_\beta$  and  $K'_\rho$  for the same model and source-receiver geometry. Note that although we construct the adjoint source using the P wave, significant non-zero S-wave sensitivity is visible in the  $K_\beta$  and  $K_\mu$  kernels. We interpret these areas of high sensitivity as P-to-S scattering locations, which affect the signal within the chosen time window. As may be observed in Fig. 12, such scattering sensitivity is especially strong at the free surface close to the receiver.

## 5.2 Acoustic sensitivity kernels

Liu & Tromp (2008) calculated global sensitivity kernels, which include sensitivity to the liquid outer core. In this section, we present acoustic sensitivity kernels for general local- or regional-scale models. Such kernels may be used, for example, in ocean acoustics, non-destructive testing and medical tomography.

For acoustic simulations, the kernels are given by

$$K_\rho = \rho^{-1} \int_0^T [\nabla \partial_t \phi^\dagger(T-t)] \cdot [\nabla \partial_t \phi(t)] dt, \quad (22)$$

$$K_\kappa = -\kappa^{-1} \int_0^T \partial_t^2 \phi^\dagger(T-t) \partial_t^2 \phi(t) dt, \quad (23)$$

where  $\phi$  and  $\phi^\dagger$  denote the acoustic scalar potential and adjoint potential, respectively. To illustrate these kernels, we use a model with acoustic and elastic regions. The model combines a water layer on top of a homogeneous elastic layer, separated by a bathymetric surface. The dimensions of the model volume are approximately 2 km  $\times$  2 km horizontally and 1 km in depth. Bathymetry is taken from a location in front of Pearl Harbor (Hawaii,

USA), with a resolution of  $\sim 11$  m. For the forward simulation, we use a pressure source in the form of an explosion with a Gaussian source-time function, and record pressure variations at the receiver. Both source and receiver are in the acoustic domain at a depth of 10 m and  $\sim 1.1$  km apart from each other. We use the simulated pressure variation within the measurement window as the pressure misfit for the adjoint source, as explained in Appendix A.1.

Fig. 13 shows the corresponding combined acoustic and elastic kernels. The kernels highlight how the pressure waveform in the chosen measurement window is affected by a head wave (a Scholte wave) traveling along the sea floor. Since the acoustic region does not support shear waves, the kernels  $K_\mu$  and  $K_\beta$  are zero in this upper domain. However, they do exhibit non-zero sensitivity in the elastic domain, due to P-to-S coupling along the sea floor.

### 5.3 Noise sensitivity kernels

As demonstrated by Tromp et al. (2010), noise cross-correlation sensitivity kernels may also be calculated based on an adjoint method, and the new package has the necessary capabilities to perform such calculations. Consider two receivers located at  $\mathbf{x}^\alpha$  and  $\mathbf{x}^\beta$ . In seismic interferometry, ensemble sensitivity kernels are calculated in terms of interactions between an ensemble forward wavefield  $\Phi^\alpha$ , generated at location  $\mathbf{x}^\alpha$ , and an ensemble adjoint wavefield  $\Phi^{\dagger\alpha\beta}$ , generated at  $\mathbf{x}^\beta$  and triggered by the differences between simulated and observed ensemble-averaged cross correlations at  $\mathbf{x}^\alpha$  and  $\mathbf{x}^\beta$ . The isotropic ensemble sensitivity kernels are given by

$$\langle K_\rho \rangle = - \int \rho [\Phi^{\dagger\alpha\beta}(-t) \cdot \partial_t^2 \Phi^\alpha(t) + \Phi^{\dagger\beta\alpha}(-t) \cdot \partial_t^2 \Phi^\beta(t)] dt, \quad (24)$$

$$\langle K_\mu \rangle = - \int 2\mu [\mathbf{D}^{\dagger\alpha\beta}(-t) : \mathbf{D}^\alpha(t) + \mathbf{D}^{\dagger\beta\alpha}(-t) : \mathbf{D}^\beta(t)] dt, \quad (25)$$

$$\langle K_\kappa \rangle = - \int \kappa [\nabla \cdot \Phi^{\dagger\alpha\beta}(-t) \nabla \cdot \Phi^\alpha(t) + \nabla \cdot \Phi^{\dagger\beta\alpha}(-t) \nabla \cdot \Phi^\beta(t)] dt, \quad (26)$$

where

$$\mathbf{D}^\alpha = \frac{1}{2} [\nabla \Phi^\alpha + (\nabla \Phi^\alpha)^T] - \frac{1}{3} (\nabla \cdot \Phi^\alpha) \mathbf{I}, \quad (27)$$

$$\mathbf{D}^{\dagger\alpha\beta} = \frac{1}{2} [\nabla \Phi^{\dagger\alpha\beta} + (\nabla \Phi^{\dagger\alpha\beta})^T] - \frac{1}{3} (\nabla \cdot \Phi^{\dagger\alpha\beta}) \mathbf{I}, \quad (28)$$

denote the traceless ensemble strain deviator and corresponding adjoint.

Figure 14 shows the isotropic kernel  $\langle K_\beta \rangle$  calculated according to eq. (20) using the primary isotropic ensemble sensitivity kernels given above. Plotted are the two contributions from ensemble wavefields generated at the first receiver location,  $\mathbf{x}^\alpha$ , and the second receiver location,  $\mathbf{x}^\beta$ , as well as the combined ensemble sensitivity kernel  $\langle K_\beta \rangle$ , which is the sum of the two contributions. The two receivers are placed at a distance of 65 km from each other on top of a homogeneous block model with dimensions of 134 km  $\times$  134 km horizontally and 60 km in depth. We smooth the kernel contributions using a 3D Gaussian filter with a standard deviation of 2 km in the horizontal and vertical directions. Note that these noise sensitivity kernels exhibit strong three-dimensional variability. Depth sensitivity is controlled by the period range (5–100 s in this example).

## 6 CONCLUSIONS AND FUTURE WORK

We have taken advantage of recent advances in high-performance computing, fully unstructured hexahedral meshing, load balancing and mesh partitioning to facilitate forward and adjoint simulations of seismic wave propagation in coupled fluid and solid domains. Our new open source software package, [SPECFEM3D](#) Version 2.0 ‘Sesame’, performs acoustic and (an)elastic simulations of seismic wave propagation in complex geological models. Hexahedral meshes may be generated based on packages such as [CUBIT](#), [Abaqus](#), [ANSYS](#), [GOCAD](#), [GiD](#), [Gmsh](#), [TrueGrid](#) or [Salome](#), but the simple in-house mesher used in previous versions of [SPECFEM3D](#) remains available for back-compatibility.

Partitioning and load balancing meshes may be accomplished based on graph partitioning software, such as [SCOTCH](#). By coupling acoustic and (an)elastic wave propagation, we are able to calculate related sensitivity kernels, which are useful for waveform inversions in off-shore exploration seismology, ocean acoustics, non-destructive testing and medical tomography. Attenuation is important on all scales of seismic wave propagation and is accommodated based on a series of standard linear solids. In particular for simulations in medical tomography, strong attenuation and related dispersion play a dominant role. Finally, the new package can be used to calculate finite-frequency noise cross-correlation

sensitivity kernels, which may be used for seismic interferometry. In future work, we will add C-PML and GPU support to the package. Visco-plastic and non-linear elastic rheologies (e.g., Xu et al. 2003; di Prisco et al. 2007) are accommodated by the [GeoELSE](#) software package (Stupazzini et al. 2009; Chaljub et al. 2010), and we will consider such non-linear constitutive relationships in future releases of [SPECFEM3D](#).

The next grand challenge involves the development of 3D seismic imaging and inversion tools for the characterization of earthquakes, Earth ‘noise’, and mapping of Earth’s interior on all scales, that is, to address the seismological inverse problem. The goal is to harness the power of forward and adjoint modeling tools, such as [SPECFEM3D](#), together with modern computers to enhance the quality of images of Earth’s interior and the earthquake rupture process. Most traditional tomographic methods utilize traveltimes or phase information measured by comparing data with simulations, and interpret such measurements based on ray theory or other approximate methods. Because of the limitations of these approximate theories, only parts of seismograms can be used, and initial models are generally restricted to be spherically symmetric. With the new generation of modeling tools we can go beyond classical tomography by using fully 3D initial models (e.g., Akçelik et al. 2002, 2003; Askan et al. 2007; Chen et al. 2007; Fichtner et al. 2009b; Fichtner 2010), and utilizing as much information contained in seismograms as possible (e.g., Maggi et al. 2009; Valentine & Woodhouse 2010). Our approach will be to minimize frequency-dependent phase and amplitude differences between simulated and observed seismograms based on adjoint techniques in combination with conjugate gradient methods, an approach we refer to as ‘adjoint tomography’ (Tape et al. 2009, 2010). The development of such capabilities will affect the fields of exploration geophysics, regional & global seismology, ocean acoustics, non-destructive testing, medical tomography and helioseismology.

## ACKNOWLEDGMENTS

We thank two anonymous reviewers for comments which improved the manuscript. All simulations were performed on a Dell cluster built and maintained by the Princeton Institute for Computational Science & Engineering (USA). The open source spectral-

element software package [SPECFEM3D](#) Version 2.0 ‘Sesame’ used for this article is available for download via the Computational Infrastructure for Geodynamics ([CIG](#)). 3D graphics were produced with the open source visualization application [Paraview](#). We acknowledge support by the US National Science Foundation under grant EAR-0711177.

## REFERENCES

- Acosta Minolia, C. A. & Kopriva, D. A., 2011. Discontinuous Galerkin spectral element approximations on moving meshes, *J. Comput. Phys.*, **230**(5), 1876–1902.
- Ainsworth, M., Monk, P., & Muniz, W., 2006. Dispersive and dissipative properties of discontinuous Galerkin finite element methods for the second-order wave equation, *Journal of Scientific Computing*, **27**(1), 5–40.
- Akçelik, V., Biros, G., & Ghattas, O., 2002. Parallel multiscale Gauss–Newton–Krylov methods for inverse wave propagation, *Proc. ACM/IEEE Supercomputing SC’2002 conference*, published on CD-ROM and at [www.sc-conference.org/sc2002](http://www.sc-conference.org/sc2002).
- Akçelik, V., Bielak, J., Biros, G., Epanomeritakis, I., Fernández, A., Ghattas, O., Kim, E. J., López, J., O’Hallaron, D., Tu, T., & Urbanic, J., 2003. High resolution forward and inverse earthquake modeling on terascale computers, *Proc. ACM/IEEE Supercomputing SC’2003 conference*, published on CD-ROM and at [www.sc-conference.org/sc2003](http://www.sc-conference.org/sc2003).
- ANSYS, 2011. *ANSYS Academic Research Workbench Platform*, ANSYS, Inc., Canonsburg, PA, USA, release 12.1 edn.
- Arnold, D. N., 1982. An interior penalty finite element method with discontinuous elements, *SIAM Journal on Numerical Analysis*, **19**(4), 742–760.
- Askan, A., Akcelik, V., Bielak, J., & Ghattas, O., 2007. Full waveform inversion for seismic velocity and anelastic losses in heterogeneous structures, *Bull. seism. Soc. Am.*, **97**(6), 1990–2008.
- Benjemaa, M., Glinsky-Olivier, N., Cruz-Atienza, V. M., Virieux, J., & Piperno, S., 2007. Dynamic non-planar crack rupture by a finite volume method, *Geophys. J. Int.*, **171**(1), 271–285.
- Benjemaa, M., Glinsky-Olivier, N., Cruz-Atienza, V. M., & Virieux, J., 2009. 3D dynamic rupture simulation by a finite volume method, *Geophys. J. Int.*, **178**(1), 541–560.
- Bergeaud, V., Lefebvre, V., & Rossignon, E., 2010. *SALOME The open source integration platform for numerical simulation*, Open Cascade, Guyancourt, France.
- Bernacki, M., Lanteri, S., & Piperno, S., 2006. Time-domain parallel simulation of hetero-

- geneous wave propagation on unstructured grids using explicit, nondiffusive, discontinuous Galerkin methods, *J. Comput. Acoust.*, **14**(1), 57–81.
- Bernardi, C., Maday, Y., & Patera, A. T., 1994. A new nonconforming approach to domain decomposition: the Mortar element method, in *Nonlinear partial differential equations and their applications*, Séminaires du Collège de France, pp. 13–51, Pitman, Paris.
- Blacker, T., Knupp, P., Lober, R. R., Melander, D., Sjaardema, G. D., Sample, W. A., Smith, M. K., Tautges, T. J., White, D. R., Benzley, S., Kerr, R., Jankovich, S. R., McRae, D. B., & Panthaki, M., 1994. *CUBIT Mesh Generation Environment Users Manual Vol. 1*, Sandia National Laboratories, Albuquerque, NM.
- Canuto, C., Hussaini, M. Y., Quarteroni, A., & Zang, T. A., 1988. *Spectral methods in fluid dynamics*, Springer-Verlag, New York, USA.
- Capdeville, Y., Chaljub, E., Villette, J. P., & Montagner, J. P., 2003. Coupling the spectral element method with a modal solution for elastic wave propagation in global Earth models, *Geophys. J. Int.*, **152**, 34–67.
- Carcione, J. M., 2007. *Wave fields in real media: Theory and numerical simulation of wave propagation in anisotropic, anelastic, porous and electromagnetic media*, Elsevier Science, Amsterdam, The Netherlands, 2nd edn.
- Carcione, J. M. & Wang, P. J., 1993. A Chebyshev collocation method for the wave equation in generalized coordinates, *Comp. Fluid Dyn. J.*, **2**, 269–290.
- Carcione, J. M., Kosloff, D., & Kosloff, R., 1988a. Wave propagation simulation in an elastic anisotropic (transversely isotropic) solid, *Q. J. Mech. Appl. Math.*, **41**(3), 319–345.
- Carcione, J. M., Kosloff, D., & Kosloff, R., 1988b. Wave propagation simulation in a linear viscoelastic medium, *Geophys. J. Int.*, **95**, 597–611.
- Carcione, J. M., Kosloff, D., Behle, A., & Seriani, G., 1992. A spectral scheme for wave propagation simulation in 3-D elastic-anisotropic media, *Geophysics*, **57**(12), 1593–1607.
- Carrington, L., Komatitsch, D., Laurenzano, M., Tikir, M., Michéa, D., Le Goff, N., Snavely, A., & Tromp, J., 2008. High-frequency simulations of global seismic wave propagation using SPECFEM3D\_GLOBE on 62 thousand processor cores, *Proceedings of the ACM/IEEE Supercomputing SC’2008 conference*, pp. 1–11, Article #60, Gordon Bell Prize finalist article.
- Casadei, F. & Gabellini, E., 1997. Implementation of a 3D coupled Spectral Element solver for wave propagation and soil-structure interaction simulations, Tech. rep., European Commission Joint Research Center Report EUR17730EN, Ispra, Italy.
- Casarotti, E., Stupazzini, M., Lee, S., Komatitsch, D., Piersanti, A., & Tromp, J., 2008. CUBIT and seismic wave propagation based upon the spectral-element method: An advanced unstructured mesher for complex 3D geological media, in *Proceedings of the 16th International*

- Meshing Roundtable*, vol. 5B.4, pp. 579–597.
- Caumon, G., Collon-Drouaillet, P., le Carlier de Veslud, C., Sausse, J., & Viseur, S., 2009. Surface-based 3D modeling of geological structures, *Mathematical Geosciences*, **41**(9), 927–945.
- Chaljub, E., 2000. *Modélisation numérique de la propagation d'ondes sismiques en géométrie sphérique : application à la sismologie globale (Numerical modeling of the propagation of seismic waves in spherical geometry: application to global seismology)*, Ph.D. thesis, Université Paris VII Denis Diderot, Paris, France.
- Chaljub, E. & Valette, B., 2004. Spectral element modelling of three-dimensional wave propagation in a self-gravitating Earth with an arbitrarily stratified outer core, *Geophys. J. Int.*, **158**, 131–141.
- Chaljub, E., Capdeville, Y., & Villette, J. P., 2003. Solving elastodynamics in a fluid-solid heterogeneous sphere: a parallel spectral-element approximation on non-conforming grids, *J. Comput. Phys.*, **187**(2), 457–491.
- Chaljub, E., Cornou, C., Guéguen, P., Causse, M., & Komatitsch, D., 2005. Spectral-element modeling of 3D wave propagation in the alpine valley of Grenoble, France, in *Geophysical Research Abstracts*, vol. 7, 05225, EGU 2nd general assembly, Wien, Austria.
- Chaljub, E., Komatitsch, D., Villette, J. P., Capdeville, Y., Valette, B., & Festa, G., 2007. Spectral element analysis in seismology, in *Advances in wave propagation in heterogeneous media*, vol. 48 of **Advances in Geophysics**, pp. 365–419, eds Wu, R.-S. & Maupin, V., Elsevier - Academic Press, London, UK.
- Chaljub, E., Moczo, P., Tsuno, S., Bard, P.-Y., Kristek, J., Käser, M., Stupazzini, M., & Kristekova, M., 2010. Quantitative comparison of four numerical predictions of 3D ground motion in the Grenoble valley, France, *Bull. Seismol. Soc. Am.*, **100**(4), 1427–1455.
- Chen, M. & Tromp, J., 2007. Theoretical and numerical investigations of global and regional seismic wave propagation in weakly anisotropic earth models, *Geophys. J. Int.*, **168**(3), 1130–1152.
- Chen, P., Zhao, L., & Jordan, T. H., 2007. Full 3D tomography for the crustal structure of the Los Angeles region, *Bull. seism. Soc. Am.*, **97**(4), 1094–1120.
- Chevalier, C. & Pellegrini, F., 2008. PT-SCOTCH: A tool for efficient parallel graph ordering, *Parallel Computing*, **34**(6-8), 318–331.
- Clayton, R. & Engquist, B., 1977. Absorbing boundary conditions for acoustic and elastic wave equations, *Bull. Seismol. Soc. Am.*, **67**, 1529–1540.
- Cockburn, B., Karniadakis, G. E., & Shu, C.-W., 2000. *Discontinuous Galerkin Methods: Theory, Computation and Applications*, Springer, Heidelberg, Germany.

- Cohen, G., 2002. *Higher-order numerical methods for transient wave equations*, Springer-Verlag, Berlin, Germany.
- Cohen, G., Joly, P., & Tordjman, N., 1993. Construction and analysis of higher-order finite elements with mass lumping for the wave equation, in *Proceedings of the second international conference on mathematical and numerical aspects of wave propagation*, pp. 152–160, SIAM, Philadelphia, Pennsylvania, USA.
- Danielson, K. T. & Namburu, R. R., 1998. Nonlinear dynamic finite element analysis on parallel computers using Fortran90 and MPI, *Advances in Engineering Software*, **29**(3-6), 179–186.
- Day, S. M. & Bradley, C., 2001. Memory-efficient simulation of anelastic wave propagation, *Bull. Seismol. Soc. Am.*, **91**, 520–531.
- De Basabe, J. D. & Sen, M. K., 2007. Grid dispersion and stability criteria of some common finite-element methods for acoustic and elastic wave equations, *Geophysics*, **72**(6), T81–T95.
- De Basabe, J. D. & Sen, M. K., 2010. Stability of the high-order finite elements for acoustic or elastic wave propagation with high-order time stepping, *Geophys. J. Int.*, **181**(1), 577–590.
- De Basabe, J. D., Sen, M. K., & Wheeler, M. F., 2008. The interior penalty discontinuous Galerkin method for elastic wave propagation: grid dispersion, *Geophys. J. Int.*, **175**(1), 83–93.
- de la Puente, J., Ampuero, J. P., & Käser, M., 2009. Dynamic rupture modeling on unstructured meshes using a discontinuous Galerkin method, *J. Geophys. Res.*, **114**, B10302.
- Delavaud, E., Cupillard, P., Festa, G., & Villette, J.-P., 2006. 3D spectral element method simulations of the seismic response in the Caracas basin, in *Proc. of the Third International Symposium on the Effects of Surface Geology on Seismic Motion*, vol. 1, pp. 512–522, Grenoble, France.
- Deville, M. O., Fischer, P. F., & Mund, E. H., 2002. *High-Order Methods for Incompressible Fluid Flow*, Cambridge University Press, Cambridge, United Kingdom.
- di Prisco, C., Stupazzini, M., & Zambelli, C., 2007. Nonlinear SEM numerical analyses of dry dense sand specimens under rapid and dynamic loading, *Int. J. Numer. Anal. Meth. Geomech.*, **31**, 757–788.
- Dumbser, M. & Käser, M., 2006. An arbitrary high-order discontinuous Galerkin method for elastic waves on unstructured meshes-II. The three-dimensional isotropic case, *Geophys. J. Int.*, **167**(1), 319–336.
- Dupros, F., de Martin, F., Foerster, E., Komatitsch, D., & Roman, J., 2010. High-performance finite-element simulations of seismic wave propagation in three-dimensional non linear inelastic geological media, *Parallel Computing*, **36**(5-6), 308–325.
- Emmerich, H. & Korn, M., 1987. Incorporation of attenuation into time-domain computations

- of seismic wave fields, *Geophysics*, **52**, 1252–1264.
- Étienne, V., Chaljub, E., Virieux, J., & Glinsky, N., 2010. An hp-adaptive discontinuous Galerkin finite-element method for 3-D elastic wave modelling, *Geophys. J. Int.*, **183**(2), 941–962.
- Faccioli, E., Maggio, F., Paolucci, R., & Quarteroni, A., 1997. 2D and 3D elastic wave propagation by a pseudo-spectral domain decomposition method, *J. Seismol.*, **1**, 237–251.
- Falk, R. S. & Richter, G. R., 1999. Explicit finite element methods for symmetric hyperbolic equations, *SIAM Journal on Numerical Analysis*, **36**(3), 935–952.
- Fichtner, A., 2010. *Full seismic waveform modelling and inversion*, Springer-Verlag, Heidelberg, Germany.
- Fichtner, A., Igel, H., Bunge, H.-P., & Kennett, B. L. N., 2009a. Simulation and inversion of seismic wave propagation on continental scales based on a spectral-element method, *Journal of Numerical Analysis, Industrial and Applied Mathematics*, **4**(1-2), 11–22.
- Fichtner, A., Kennett, B. L. N., Igel, H., & Bunge, H.-P., 2009b. Full seismic waveform tomography for upper-mantle structure in the Australasian region using adjoint methods, *Geophys. J. Int.*, **179**, 1703–1725.
- Gardia-Donoro, D., Garcia-Castillo, L. E., & Gómez-Revuelto, I., 2010. An interface between an hp-adaptive finite element package and the pre- and post-processor GiD, *Finite Elements in Analysis and Design*, **46**(4), 328–338.
- Geuzaine, C. & Remacle, J. F., 2009. Gmsh: A three-dimensional finite element mesh generator with built-in pre- and post-processing facilities, *Int. J. Numer. Meth. Eng.*, **79**(11), 1309–1331.
- Giraldo, F. X., Hesthaven, J. S., & Warburton, T., 2002. Nodal high-order discontinuous Galerkin methods for the spherical shallow water equations, *J. Comput. Phys.*, **181**(2), 499–525.
- Grote, M. J., Schneebeli, A., & Schötzau, D., 2006. Discontinuous Galerkin finite element method for the wave equation, *SIAM Journal on Numerical Analysis*, **44**(6), 2408–2431.
- Hesthaven, J. S. & Teng, C. H., 2000. Stable spectral methods on tetrahedral elements, *SIAM J. Sci. Comput.*, **21**, 2352–2380.
- Hu, F. Q., Hussaini, M. Y., & Rasetarinera, P., 1999. An analysis of the discontinuous Galerkin method for wave propagation problems, *J. Comput. Phys.*, **151**(2), 921–946.
- Jarvis, A., Reuter, H., Nelson, A., & Guevara, E., 2008. Hole-filled seamless SRTM data V4.
- Karypis, G. & Kumar, V., 1998. A parallel algorithm for multilevel graph partitioning and sparse matrix ordering, *Journal of Parallel and Distributed Computing*, **48**, 71–85.
- Komatitsch, D., 1997. *Méthodes spectrales et éléments spectraux pour l'équation de*

*l’élastodynamique 2D et 3D en milieu hétérogène (Spectral and spectral-element methods for the 2D and 3D elastodynamics equations in heterogeneous media)*, Ph.D. thesis, Institut de Physique du Globe, Paris, France, 187 pages.

- Komatitsch, D., 2011. Fluid-solid coupling on a cluster of GPU graphics cards for seismic wave propagation, *Comptes Rendus de l’Académie des Sciences - Mécanique*, in press.
- Komatitsch, D. & Martin, R., 2007. An unsplit convolutional Perfectly Matched Layer improved at grazing incidence for the seismic wave equation, *Geophysics*, **72**(5), SM155–SM167.
- Komatitsch, D. & Tromp, J., 1999. Introduction to the spectral-element method for 3-D seismic wave propagation, *Geophys. J. Int.*, **139**(3), 806–822.
- Komatitsch, D. & Tromp, J., 2002a. Spectral-element simulations of global seismic wave propagation-I. Validation, *Geophys. J. Int.*, **149**(2), 390–412.
- Komatitsch, D. & Tromp, J., 2002b. Spectral-element simulations of global seismic wave propagation-II. 3-D models, oceans, rotation, and self-gravitation, *Geophys. J. Int.*, **150**(1), 303–318.
- Komatitsch, D. & Vilotte, J. P., 1998. The spectral-element method: an efficient tool to simulate the seismic response of 2D and 3D geological structures, *Bull. Seismol. Soc. Am.*, **88**(2), 368–392.
- Komatitsch, D., Coutel, F., & Mora, P., 1996. Tensorial formulation of the wave equation for modelling curved interfaces, *Geophys. J. Int.*, **127**(1), 156–168.
- Komatitsch, D., Martin, R., Tromp, J., Taylor, M. A., & Wingate, B. A., 2001. Wave propagation in 2-D elastic media using a spectral element method with triangles and quadrangles, *J. Comput. Acoust.*, **9**(2), 703–718.
- Komatitsch, D., Tsuboi, S., Ji, C., & Tromp, J., 2003. A 14.6 billion degrees of freedom, 5 teraflops, 2.5 terabyte earthquake simulation on the Earth Simulator, *Proceedings of the ACM/IEEE Supercomputing SC’2003 conference*, pp. 4–11, Gordon Bell Prize winner article.
- Komatitsch, D., Liu, Q., Tromp, J., Süss, P., Stidham, C., & Shaw, J. H., 2004. Simulations of ground motion in the Los Angeles basin based upon the spectral-element method, *Bull. Seismol. Soc. Am.*, **94**(1), 187–206.
- Komatitsch, D., Tsuboi, S., & Tromp, J., 2005. The spectral-element method in seismology, in *Seismic Earth: Array Analysis of Broadband Seismograms*, vol. 157 of **Geophysical Monograph**, pp. 205–228, eds Levander, A. & Nolet, G., American Geophysical Union, Washington DC, USA.
- Komatitsch, D., Labarta, J., & Michéa, D., 2008. A simulation of seismic wave propagation at high resolution in the inner core of the Earth on 2166 processors of MareNostrum, *Lecture Notes in Computer Science*, **5336**, 364–377.

- Komatitsch, D., Michéa, D., & Erlebacher, G., 2009. Porting a high-order finite-element earthquake modeling application to NVIDIA graphics cards using CUDA, *Journal of Parallel and Distributed Computing*, **69**(5), 451–460.
- Komatitsch, D., Erlebacher, G., Göddeke, D., & Michéa, D., 2010a. High-order finite-element seismic wave propagation modeling with MPI on a large GPU cluster, *J. Comput. Phys.*, **229**(20), 7692–7714.
- Komatitsch, D., Vinnik, L. P., & Chevrot, S., 2010b. SHdiff/SVdiff splitting in an isotropic Earth, *J. Geophys. Res.*, **115**(B7), B07312.
- Kopriva, D. A., 2006. Metric identities and the discontinuous spectral element method on curvilinear meshes, *Journal of Scientific Computing*, **26**(3), 301–327.
- Kopriva, D. A., Woodruff, S. L., & Hussaini, M. Y., 2002. Computation of electromagnetic scattering with a non-conforming discontinuous spectral element method, *Int. J. Numer. Meth. Eng.*, **53**(1), 105–122.
- Lee, S. J., Chen, H. W., Liu, Q., Komatitsch, D., Huang, B. S., & Tromp, J., 2008. Three-dimensional simulations of seismic wave propagation in the Taipei basin with realistic topography based upon the spectral-element method, *Bull. Seismol. Soc. Am.*, **98**(1), 253–264.
- Lee, S. J., Chan, Y. C., Komatitsch, D., Huang, B. S., & Tromp, J., 2009a. Effects of realistic surface topography on seismic ground motion in the Yangminshan region of Taiwan based upon the spectral-element method and LiDAR DTM, *Bull. Seismol. Soc. Am.*, **99**(2A), 681–693.
- Lee, S. J., Komatitsch, D., Huang, B. S., & Tromp, J., 2009b. Effects of topography on seismic wave propagation: An example from northern Taiwan, *Bull. Seismol. Soc. Am.*, **99**(1), 314–325.
- Legay, A., Wang, H. W., & Belytschko, T., 2005. Strong and weak arbitrary discontinuities in spectral finite elements, *Int. J. Numer. Meth. Eng.*, **64**(8), 991–1008.
- Liu, H. P., Anderson, D. L., & Kanamori, H., 1976. Velocity dispersion due to anelasticity: implications for seismology and mantle composition, *Geophys. J. Roy. Astron. Soc.*, **47**, 41–58.
- Liu, Q. & Tromp, J., 2006. Finite-frequency kernels based on adjoint methods, *Bull. Seismol. Soc. Am.*, **96**(6), 2383–2397.
- Liu, Q. & Tromp, J., 2008. Finite-frequency sensitivity kernels for global seismic wave propagation based upon adjoint methods, *Geophys. J. Int.*, **174**(1), 265–286.
- Liu, Q., Polet, J., Komatitsch, D., & Tromp, J., 2004. Spectral-element moment tensor inversions for earthquakes in Southern California, *Bull. Seismol. Soc. Am.*, **94**(5), 1748–1761.
- Maday, Y. & Patera, A. T., 1989. Spectral-element methods for the incompressible Navier-

- Stokes equations, in *State of the art survey in computational mechanics*, pp. 71–143, A. K. Noor and J. T. Oden editors.
- Maggi, A., Tape, C., Chen, M., Chao, D., & Tromp, J., 2009. An automated time window selection algorithm for seismic tomography, *Geophys. J. Int.*, **178**, 257–281.
- Mallet, J. L., 1992. *Three-Dimensional Modeling with Geoscientific Information Systems*, chap. GOCAD: a computer aided design program for geological applications, pp. 123–141, Kluwer Academic Publishers.
- Martin, R. & Couder-Castaneda, C., 2010. An improved unsplit and convolutional perfectly matched layer (CPML) absorbing technique for the Navier-Stokes equations using cut-off frequency shift, *Comput. Model. Eng. Sci.*, **63**(1), 47–77.
- Martin, R. & Komatitsch, D., 2009. An unsplit convolutional perfectly matched layer technique improved at grazing incidence for the viscoelastic wave equation, *Geophys. J. Int.*, **179**(1), 333–344.
- Martin, R., Komatitsch, D., Blitz, C., & Le Goff, N., 2008a. Simulation of seismic wave propagation in an asteroid based upon an unstructured MPI spectral-element method: blocking and non-blocking communication strategies, *Lecture Notes in Computer Science*, **5336**, 350–363.
- Martin, R., Komatitsch, D., & Ezziani, A., 2008b. An unsplit convolutional perfectly matched layer improved at grazing incidence for seismic wave equation in poroelastic media, *Geophysics*, **73**(4), T51–T61.
- Martin, R., Komatitsch, D., & Gedney, S. D., 2008c. A variational formulation of a stabilized unsplit convolutional perfectly matched layer for the isotropic or anisotropic seismic wave equation, *Comput. Model. Eng. Sci.*, **37**(3), 274–304.
- Martin, R., Komatitsch, D., Gedney, S. D., & Bruthiaux, E., 2010. A high-order time and space formulation of the unsplit perfectly matched layer for the seismic wave equation using Auxiliary Differential Equations (ADE-PML), *Comput. Model. Eng. Sci.*, **56**(1), 17–42.
- Mercerat, E. D., Vilotte, J. P., & Sánchez-Sesma, F. J., 2006. Triangular spectral-element simulation of two-dimensional elastic wave propagation using unstructured triangular grids, *Geophys. J. Int.*, **166**(2), 679–698.
- Michéa, D. & Komatitsch, D., 2010. Accelerating a 3D finite-difference wave propagation code using GPU graphics cards, *Geophys. J. Int.*, **182**(1), 389–402.
- Micikevicius, P., 2009. 3D finite-difference computation on GPUs using CUDA, in *GPGPU-2: Proceedings of the 2nd Workshop on General Purpose Processing on Graphics Processing Units*, pp. 79–84, Washington, DC, USA.
- Mitchell, S., 1996. A characterization of the quadrilateral meshes of a surface which admit a compatible hexahedral mesh of the enclosed volume, in *STACS 96*, vol. 1046 of *Lecture*

- Notes in Computer Science**, pp. 465–476, eds Puech, C. & Reischuk, R., Springer Berlin / Heidelberg.
- Moczo, P. & Kristek, J., 2005. On the rheological models used for time-domain methods of seismic wave propagation, *Geophys. Res. Lett.*, **32**, L01306.
- Monk, P. & Richter, G. R., 2005. A discontinuous Galerkin method for linear symmetric hyperbolic systems in inhomogeneous media, *Journal of Scientific Computing*, **22-23**(1-3), 443–477.
- Noble, C. R. & Nuss, L. K., 2004. Nonlinear seismic analysis of morrow point dam, in *13th World Conference on Earthquake Engineering*, Vancouver, British Columbia, Canada.
- Oliveira, S. P. & Seriani, G., 2011. Effect of element distortion on the numerical dispersion of spectral element methods, *Communications in Computational Physics*, **9**(4), 937–958.
- Paolucci, R., Faccioli, E., & Maggio, F., 1999. 3D response analysis of an instrumented hill at Matsuzaki, Japan, by a spectral method, *J. Seismol.*, **3**, 191–209.
- Patera, A. T., 1984. A spectral element method for fluid dynamics: laminar flow in a channel expansion, *J. Comput. Phys.*, **54**, 468–488.
- Pellegrini, F. & Roman, J., 1996. SCOTCH: A software package for static mapping by dual recursive bipartitioning of process and architecture graphs, *Lecture Notes in Computer Science*, **1067**, 493–498.
- Priolo, E., Carcione, J. M., & Seriani, G., 1994. Numerical simulation of interface waves by high-order spectral modeling techniques, *J. Acoust. Soc. Am.*, **95**(2), 681–693.
- Quarteroni, A., Tagliani, A., & Zampieri, E., 1998. Generalized Galerkin approximations of elastic waves with absorbing boundary conditions, *Comput. Meth. Appl. Mech. Eng.*, **163**, 323–341.
- Rainsberger, R., 2006. *TrueGrid User's Manual*, XYZ Scientific Applications, Inc., version 2.3.0 edn.
- Reed, W. H. & Hill, T. R., 1973. Triangular mesh methods for the neutron transport equation, Tech. Rep. LA-UR-73-479, Los Alamos Scientific Laboratory, Los Alamos, USA.
- Ribes, A. & Caremoli, C., 2007. Salome platform component model for numerical simulation, in *COMPSAC '07: Proceedings of the 31st Annual International Computer Software and Applications Conference*, vol. 2, pp. 553–564, IEEE Computer Society.
- Ribó, R., de Riera Pasenau, M. A., & Escolano, E., 2011. *GiD reference manual, Pre and post processing system for F.E.M. calculations*, International Center For Numerical Methods In Engineering (CIMNE).
- Richardson, J. E., Melosh, H. J., Greenberg, R. J., & O'Brien, D. P., 2005. The global effects of impact-induced seismic activity on fractured asteroid surface morphology, *Icarus*, **179**,

325–349.

- Rivi  re, B. & Wheeler, M. F., 2003. Discontinuous finite element methods for acoustic and elastic wave problems, *Contemporary Mathematics*, **329**, 271–282.
- Robertsson, J. O. A., 1996. A numerical free-surface condition for elastic/viscoelastic finite-difference modeling in the presence of topography, *Geophysics*, **61**, 1921–1934.
- Robinson, M. S., Thomas, P. C., Veverka, J., Murchie, S. L., & Wilcox, B. B., 2002. The geology of 433 Eros, *Meteoritics and Planetary Sciences*, **37**, 1651–1684.
- Savage, B., Komatitsch, D., & Tromp, J., 2010. Effects of 3D attenuation on seismic wave amplitude and phase measurements, *Bull. Seismol. Soc. Am.*, **100**(3), 1241–1251.
- Seriani, G. & Oliveira, S. P., 2008. Dispersion analysis of spectral-element methods for elastic wave propagation, *Wave Motion*, **45**, 729–744.
- Seriani, G. & Priolo, E., 1994. A spectral element method for acoustic wave simulation in heterogeneous media, *Finite Elements in Analysis and Design*, **16**, 337–348.
- Seriani, G., Priolo, E., & Pregarz, A., 1995. Modelling waves in anisotropic media by a spectral element method, in *Proceedings of the third international conference on mathematical and numerical aspects of wave propagation*, pp. 289–298, SIAM, Philadelphia, PA.
- Shepherd, J. F. & Johnson, C. R., 2008. Hexahedral mesh generation constraints, *Engineering with Computers*, **24**(3), 195 – 213.
- Sieminski, A., Liu, Q., Trampert, J., & Tromp, J., 2007a. Finite-frequency sensitivity of surface waves to anisotropy based upon adjoint methods, *Geophys. J. Int.*, **168**(3), 1153–1174.
- Sieminski, A., Liu, Q., Trampert, J., & Tromp, J., 2007b. Finite-frequency sensitivity of body waves to anisotropy based upon adjoint methods, *Geophys. J. Int.*, **171**, 368–389.
- SIMULIA, 2008. *Abaqus User’s Manual*, Dassault Systemes, Providence, RI, USA, version 6.7 edn.
- Stacey, R., 1988. Improved transparent boundary formulations for the elastic wave equation, *Bull. Seismol. Soc. Am.*, **78**(6), 2089–2097.
- Staten, M. L., Kerr, R. A., Owen, S. J., Blacker, T. D., Stupazzini, M., & Shimada, K., 2010. Unconstrained plastering—hexahedral mesh generation via advancing-front geometry decomposition, *International Journal for Numerical Methods in Engineering*, **81**, 135–171.
- Stupazzini, M., Paolucci, R., & Ig  el, H., 2009. Near-fault earthquake ground-motion simulation in the Grenoble valley by a high-performance spectral element code, *Bull. Seismol. Soc. Am.*, **99**(1), 286–301.
- Tago, J., Cruz-Atienza, V. M.,   tienne, V., Virieux, J., Benjemaa, M., & S  nchez-Sesma, F. J., 2010. 3D dynamic rupture with anelastic wave propagation using an hp-adaptive Discontinuous Galerkin method, in *Abstract S51A-1915 presented at 2010 AGU Fall Meeting*,

- San Francisco, California, USA, [www.agu.org/meetings/fm10/waisfm10.html](http://www.agu.org/meetings/fm10/waisfm10.html).
- Tape, C., Liu, Q., Maggi, A., & Tromp, J., 2009. Adjoint tomography of the southern California crust, *Science*, **325**, 988–992.
- Tape, C., Liu, Q., Maggi, A., & Tromp, J., 2010. Seismic tomography of the southern California crust based on spectral-element and adjoint methods, *Geophys. J. Int.*, **180**, 433–462.
- Tarantola, A., 1984. Inversion of seismic reflection data in the acoustic approximation, *Geophysics*, **49**, 1259–1266.
- Tarantola, A., 1987. *Inverse problem theory: methods for data fitting and model parameter estimation*, Elsevier Science Publishers, Amsterdam, Netherlands.
- Taylor, M. A. & Wingate, B. A., 2000. A generalized diagonal mass matrix spectral element method for non-quadrilateral elements, *Appl. Num. Math.*, **33**, 259–265.
- Tromp, J., Tape, C., & Liu, Q., 2005. Seismic tomography, adjoint methods, time reversal and banana-doughnut kernels, *Geophys. J. Int.*, **160**(1), 195–216.
- Tromp, J., Komatitsch, D., & Liu, Q., 2008. Spectral-element and adjoint methods in seismology, *Communications in Computational Physics*, **3**(1), 1–32.
- Tromp, J., Luo, Y., Hanasoge, S., & Peter, D., 2010. Noise cross-correlation sensitivity kernels, *Geophys. J. Int.*, **183**, 791–819.
- Tsuboi, S., Komatitsch, D., Ji, C., & Tromp, J., 2003. Spectral-element simulations of the November 3, 2002, Denali, Alaska earthquake on the Earth Simulator, *Phys. Earth Planet. In.*, **139**(3-4), 305–313.
- Valentine, A. & Woodhouse, J., 2010. Approaches to automated data selection for global seismic tomography, *Geophys. J. Int.*, **182**, 1001–1012.
- van Wijk, K., Komatitsch, D., Scales, J. A., & Tromp, J., 2004. Analysis of strong scattering at the micro-scale, *J. Acoust. Soc. Am.*, **115**(3), 1006–1011.
- Vos, P. E. J., Sherwin, S. J., & Kirby, R. M., 2010. From  $h$  to  $p$  efficiently: Implementing finite and spectral/ $hp$  element methods to achieve optimal performance for low- and high-order discretisations, *J. Comput. Phys.*, **229**, 5161–5181.
- White, D. R., Mingwu, L., Benzley, S. E., & Sjaardema, G. D., 1995. Automated hexahedral mesh generation by virtual decomposition, in *Proceedings of the 4th International Meshing Roundtable*, pp. 165–176.
- Wilcox, L. C., Stadler, G., Burstedde, C., & Ghattas, O., 2010. A high-order discontinuous Galerkin method for wave propagation through coupled elastic-acoustic media, *J. Comput. Phys.*, **229**(24), 9373–9396.
- Wingate, B. A. & Boyd, J. P., 1996. Spectral element methods on triangles for geophysical fluid dynamics problems, in *Proceedings of the Third International Conference on Spectral*

and High-order Methods, pp. 305–314, Houston J. Mathematics, Houston, Texas.

Xu, J., Bielak, J., Ghattas, O., & Wang, J., 2003. Three-dimensional nonlinear seismic ground motion modeling in inelastic basins, *Phys. Earth Planet. In.*, **137**(1-4), 81–95.

## A ACOUSTIC ADJOINT EQUATIONS

### A.1 Pressure waveform misfit kernels

For acoustic tomographic studies, it is convenient to define a pressure misfit function

$$\chi = \frac{1}{2} \sum_i \int ||p_i^{\text{syn}}(\mathbf{m}) - p_i^{\text{obs}}||^2 dt, \quad (29)$$

where  $p_i^{\text{syn}}$  is the numerically computed pressure and  $p_i^{\text{obs}}$  the observed pressure at location  $\mathbf{x}_i$ . The variation in pressure may be written in terms of the variation in the potential  $\phi$  as

$$\delta p = -\partial_t^2 \delta \phi, \quad (30)$$

which follows from the definition of the scalar potential  $\phi$  in eq. (11). The corresponding action in the acoustic case is given by

$$\chi = \frac{1}{2} \sum_i \int ||p_i^{\text{syn}} - p_i^{\text{obs}}||^2 dt - \int \int_{\Omega} \lambda [\kappa^{-1} \partial_t^2 \phi - \nabla \cdot (\rho^{-1} \nabla \phi) - f] d^3 \mathbf{x} dt, \quad (31)$$

where  $\lambda$  denotes a scalar Lagrange multiplier. Setting  $\Delta p_i = p_i^{\text{syn}} - p_i^{\text{obs}}$  and taking the variation of the action, we obtain

$$\begin{aligned} \delta \chi = & \sum_i \int \Delta p_i \delta p_i dt - \int \int_{\Omega} [\delta \kappa^{-1} \lambda \partial_t^2 \phi - \nabla \cdot (\delta \rho^{-1} \lambda \nabla \phi) - \lambda \delta f] d^3 \mathbf{x} dt \\ & - \int \int_{\Omega} [\kappa^{-1} \partial_t^2 \lambda - \nabla \cdot (\rho^{-1} \nabla \lambda)] \delta \phi d^3 \mathbf{x} dt - \int \int_{\partial \Omega} \hat{\mathbf{n}} \cdot (\rho^{-1} \nabla \lambda) \delta \phi d^2 \mathbf{x} dt. \end{aligned} \quad (32)$$

Since eq. (32) must be stationary when no model perturbations are present, i.e.,  $\delta \rho = 0$ ,

$\delta\kappa = 0$  and  $\delta f = 0$ , we obtain

$$\begin{aligned} & \int \int_{\Omega} [\kappa^{-1} \partial_t^2 \lambda - \nabla \cdot (\rho^{-1} \nabla \lambda)] \delta\phi d^3x dt \\ &= \int \int_{\Omega} \sum_i \Delta p_i \delta(\mathbf{x} - \mathbf{x}_i) \delta p d^3x dt - \int \int_{\partial\Omega} \hat{\mathbf{n}} \cdot (\rho^{-1} \nabla \lambda) \delta\phi d^2x dt \\ &= - \int \int_{\Omega} \sum_i \Delta p_i \delta(\mathbf{x} - \mathbf{x}_i) \partial_t^2 \delta\phi d^3x dt - \int \int_{\partial\Omega} \rho^{-1} \hat{\mathbf{n}} \cdot \nabla \lambda \delta\phi d^2x dt \\ &= - \int \int_{\Omega} \sum_i \partial_t^2 \Delta p_i \delta(\mathbf{x} - \mathbf{x}_i) \delta\phi d^3x dt - \int \int_{\partial\Omega} \rho^{-1} \hat{\mathbf{n}} \cdot \nabla \lambda \delta\phi d^2x dt, \end{aligned} \quad (33)$$

where  $\mathbf{x}_i$  is the station location of the corresponding  $i$ th measurement. Note that the last integration by parts of the first term is valid under the assumption that  $\Delta p_i$  and  $\partial_t \Delta p_i$  vanish at the limits of the time integration, i.e., for a given measurement window  $[0, T]$ ,  $\Delta p_i(\mathbf{x}, 0) = \Delta p_i(\mathbf{x}, T) = 0$  and  $\partial_t \Delta p_i(\mathbf{x}, 0) = \partial_t \Delta p_i(\mathbf{x}, T) = 0$ . This is generally true because we taper the ends of the misfit window.

Let us define the adjoint scalar potential as

$$\phi^\dagger(\mathbf{x}, t) \equiv \lambda(\mathbf{x}, T - t). \quad (34)$$

It follows from (33) that  $\phi^\dagger$  must satisfy the adjoint wave equation

$$\kappa^{-1} \partial_t^2 \phi^\dagger - \nabla \cdot (\rho^{-1} \nabla \phi^\dagger) = f^\dagger, \quad (35)$$

where the adjoint source is given by

$$f^\dagger(\mathbf{x}, t) = - \sum_i \partial_t^2 \Delta p_i(T - t) \delta(\mathbf{x} - \mathbf{x}_i). \quad (36)$$

The initial conditions for the adjoint potential must satisfy  $\phi^\dagger(T) = 0$  and  $\partial_t \phi^\dagger(T) = 0$ . The corresponding fluid-solid boundary conditions involve terms with  $\rho^{-1} \hat{\mathbf{n}} \cdot \nabla \phi^\dagger$ . For acoustic simulations, there is no shear contribution and we may set  $K_\mu = 0$ . Using

$$\nabla \cdot \mathbf{s} = -\kappa^{-1} p = \kappa^{-1} \partial_t^2 \phi, \quad (37)$$

$$\nabla \cdot \mathbf{s}^\dagger = \kappa^{-1} \partial_t^2 \phi^\dagger, \quad (38)$$

the kernel  $K_\kappa$  given in eq. (18) becomes

$$K_\kappa = - \int_0^T \kappa^{-1} \partial_t^2 \phi^\dagger(T - t) \partial_t^2 \phi(t) dt. \quad (39)$$

It is this last kernel expression that is actually implemented, since the values for  $\partial_t^2 \phi$

and  $\partial_t^2 \phi^\dagger$  are obtained at each time step in the Newark time scheme used to propagate acoustic waves.

## A.2 Pressure travelttime adjoint sources

Instead of measuring waveform misfits, one may also define a travelttime misfit for pressure signals, i.e.,

$$\chi = \frac{1}{2} \sum_i \|T_i^{\text{syn}}(\mathbf{m}) - T_i^{\text{obs}}\|^2, \quad (40)$$

where  $T_i^{\text{syn}}(\mathbf{m})$  denotes the arrival time in the synthetic pressure records computed for model  $\mathbf{m}$ , and  $T_i^{\text{obs}}$  the arrival time of the observed pressure wave. The variation in travelttime  $\delta T$  may be written to first order in terms of perturbations in pressure as  $\delta p$  (Hung & Dahlen 2000)

$$\delta T = \frac{1}{N} \int \partial_t p \delta p dt, \quad (41)$$

where  $N = \int p \partial_t^2 p dt$ . Using  $\delta p = -\partial_t^2 \delta \phi$ , this leads to

$$\delta T = -\frac{1}{N} \int \partial_t p \partial_t^2 \delta \phi dt. \quad (42)$$

Defining  $\Delta T_i \equiv T_i^{\text{syn}}(\mathbf{m}) - T_i^{\text{obs}}$ , the variation of the action becomes

$$\sum_i \Delta T_i \delta T_i = -\sum_i \frac{1}{N} \Delta T_i \int \partial_t p \partial_t^2 \delta \phi dt \quad (43)$$

$$= -\int \int_{\Omega} \sum_i \frac{1}{N} \Delta T_i \delta(\mathbf{x} - \mathbf{x}_i) \partial_t p \partial_t^2 \delta \phi d^3 \mathbf{x} dt. \quad (44)$$

Under the assumption that  $\partial_t p(0) = \partial_t p(T) = 0$  and  $\partial_t^2 p(0) = \partial_t^2 p(T) = 0$  (which can be achieved by carefully selecting and tapering the measurement time windows), we find after some further manipulation that the adjoint source for a travelttime misfit between observed and simulated pressure signals is given by

$$f^\dagger(\mathbf{x}, t) = -\sum_i \frac{1}{N} \Delta T_i \partial_t^3 p(\mathbf{x}, T - t) \delta(\mathbf{x} - \mathbf{x}_i). \quad (45)$$

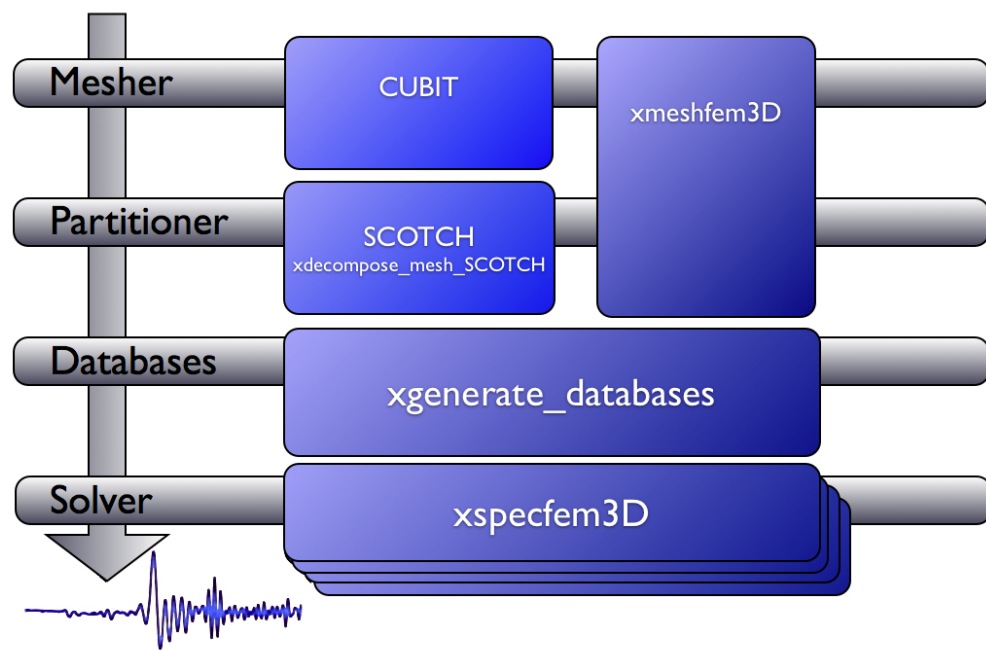


**Figure 1.** Workflow for running spectral-element simulations with [SPECFEM3D](#) Version 2.0 ‘Sesame’.

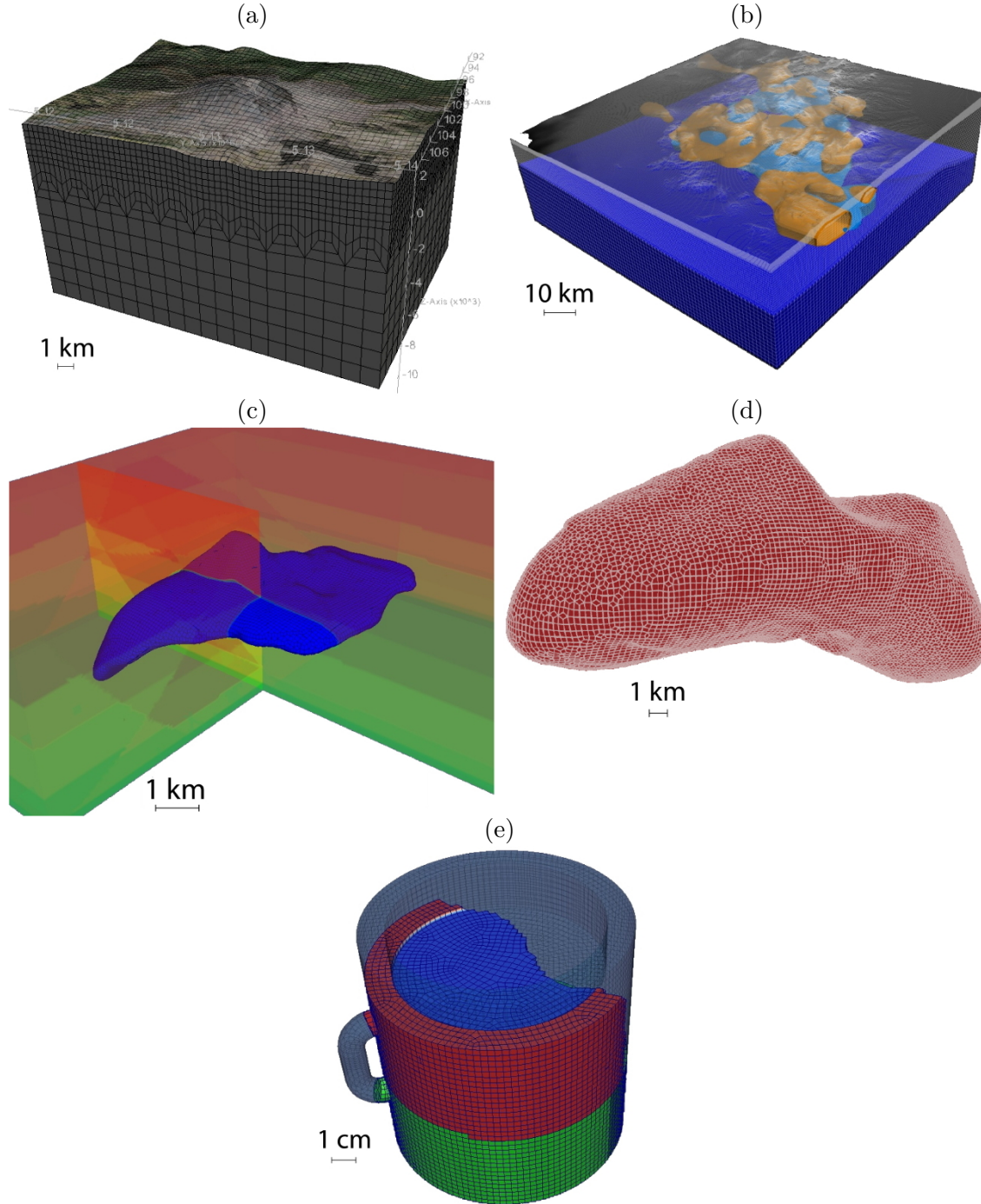


**Figure 2.** Mesh examples: (a) Mount St. Helens meshed by hexahedral elements. The mesh honors surface topography and includes a mesh tripling layer in the middle of the model. The smallest element size is approximately 280 m. (b) L’Aquila, Italy, region discretized for high-frequency simulations. The mesh honors surface and Moho topography and includes two mesh tripling layers. The yellow and blue volumes denote slower and faster than average wavespeeds, respectively. (c) Salt dome body meshed inside an exploration model for a SEG/EAGE benchmark test. (d) 3D hexahedral mesh of the asteroid 433-Eros. (e) Arbitrarily-shaped mesh for coupled solid-fluid simulations involving a coffee cup.

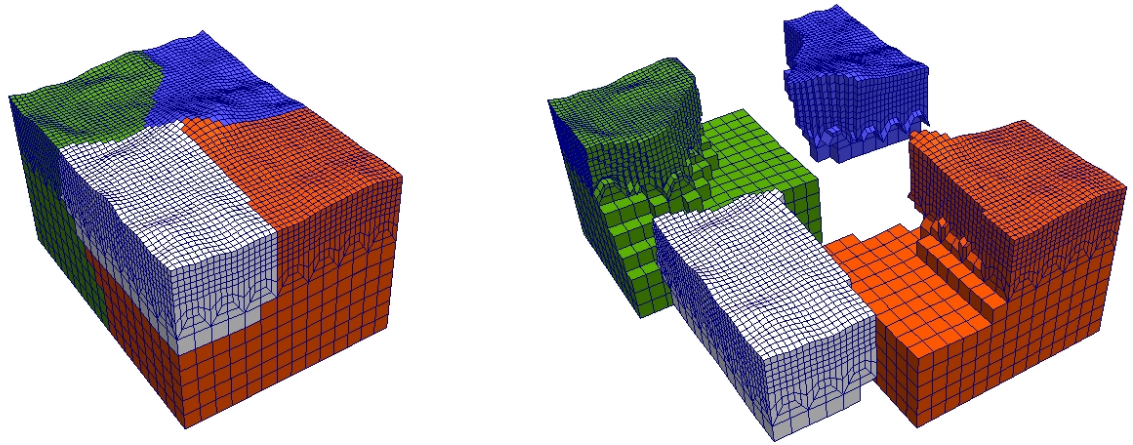


**Figure 3.** Mount St. Helens mesh partitioned and load balanced to run in parallel on four cores. The four partitions are indicated by different colors.

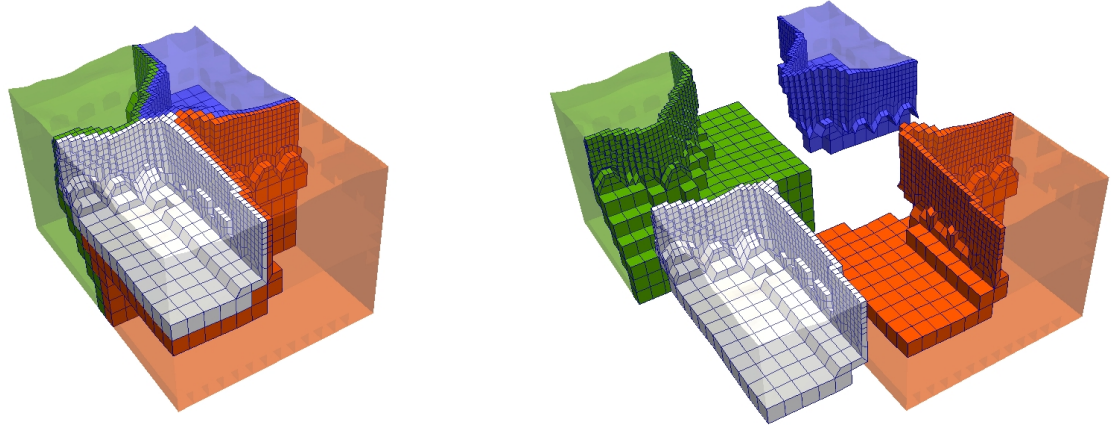


**Figure 4.** Outer (highlighted) and inner (transparent colors) elements for the mesh shown in Figure 3. Outer elements have at least one point in common with an element from another slice and must therefore be computed first, before initiating non-blocking MPI communications. While MPI messages are traveling across the computer network, simultaneous computations are performed on inner elements. Non-blocking MPI communication is crucial to obtain good scaling results for simulations running on a large number of parallel cores.

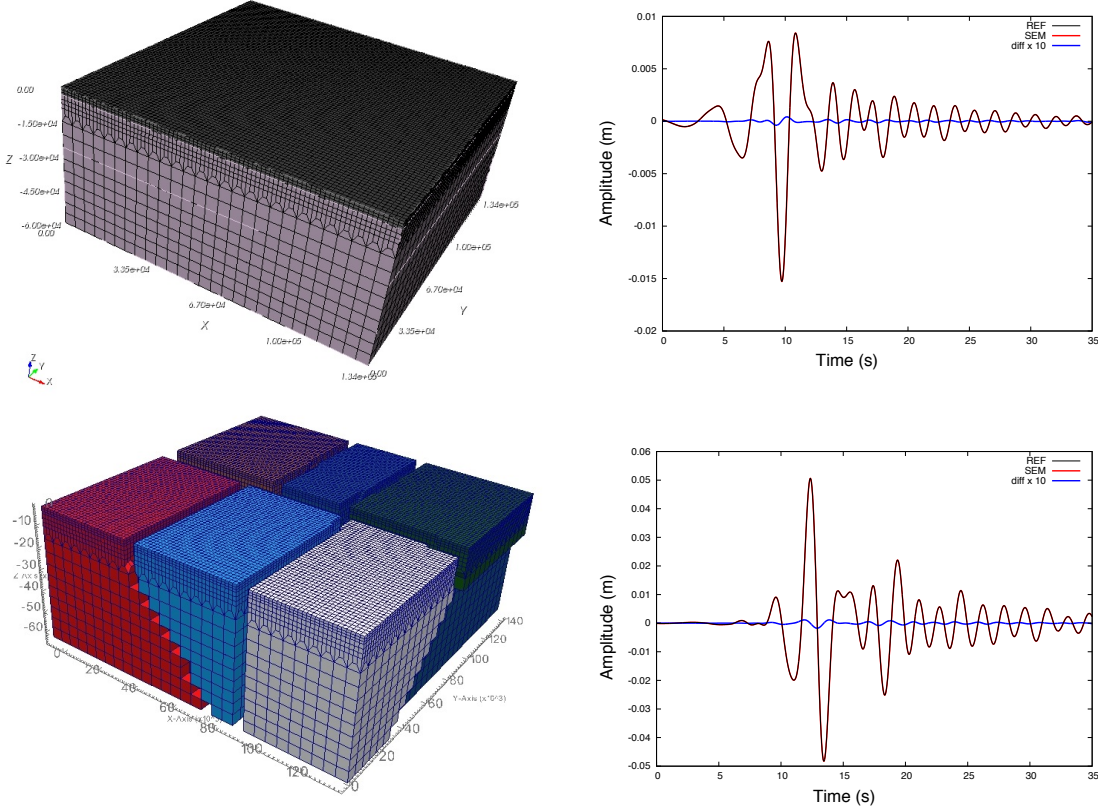


**Figure 5.** Validation for a two-layer mesh (left, top), using six partitions (left, bottom), and seismograms recorded at the surface at horizontal distances of 2.39 km (right, top) and 31.11 km (right, bottom). Plotted are radial displacements (SEM, red) against reference solutions (REF, black) from Komatitsch & Tromp (1999), as well as their exaggerated differences (blue) .

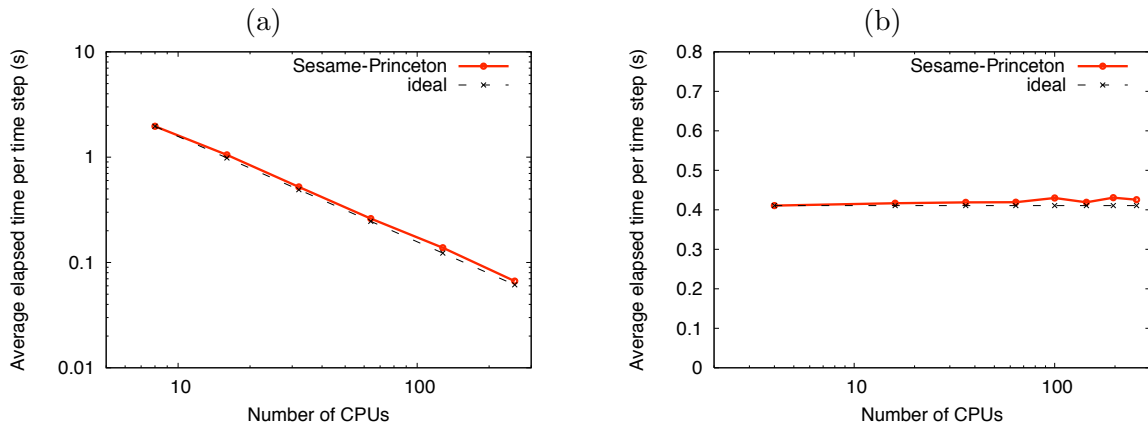


**Figure 6.** CPU scaling results for the model shown in Fig. 5, (a) using a fixed total problem size (strong scaling) and (b) a fixed problem size per processor (weak scaling) for up to 256 cores. Perfect weak scaling deviates slightly from a straight line, because a larger number of processors involves more MPI buffers and therefore more computational overhead.

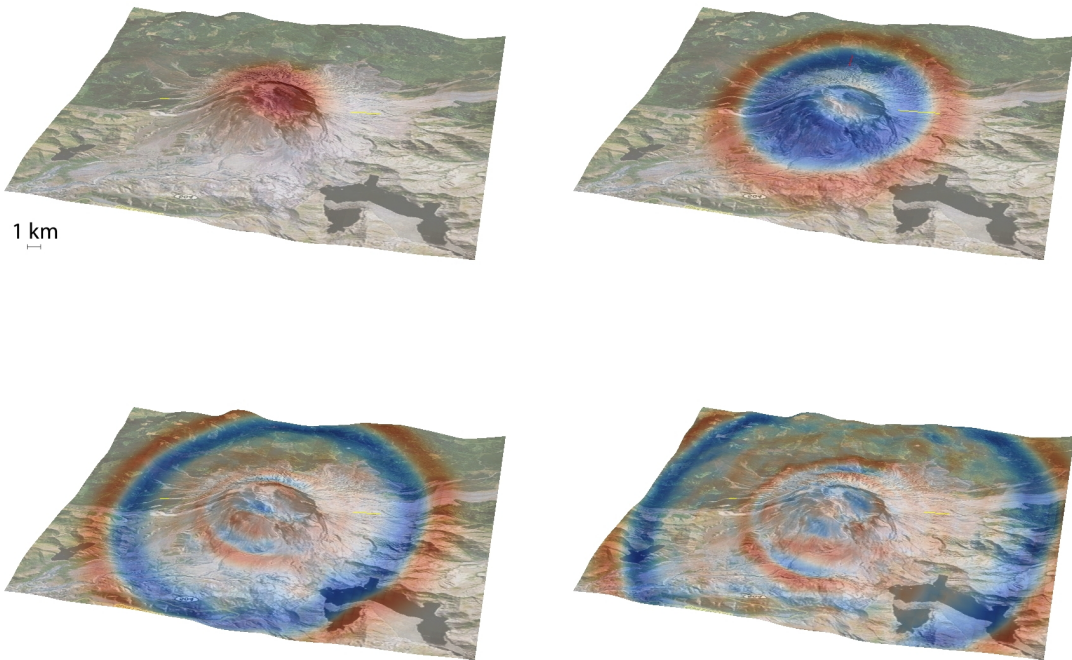


**Figure 7.** Wavefield snapshots around Mount St. Helens. Plotted are vertical displacements (up/down colored red/blue respectively) at the free surface of the model.

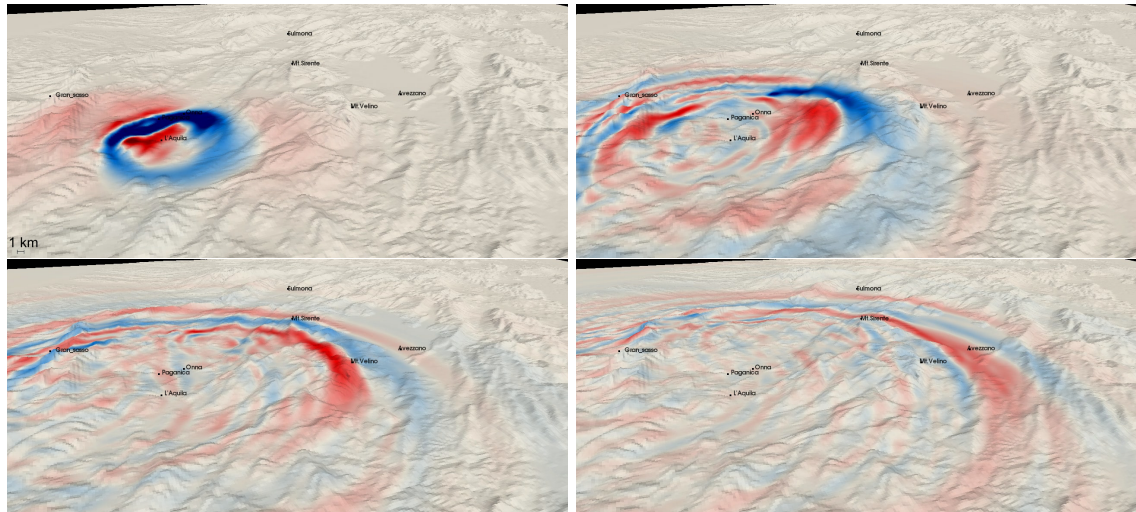


**Figure 8.** Wavefield snapshots for the April 6, 2009, L'Aquila earthquake, taken after 6 s, 11 s, 16 s and 21 s. Plotted are vertical displacements (up/down as red/blue).

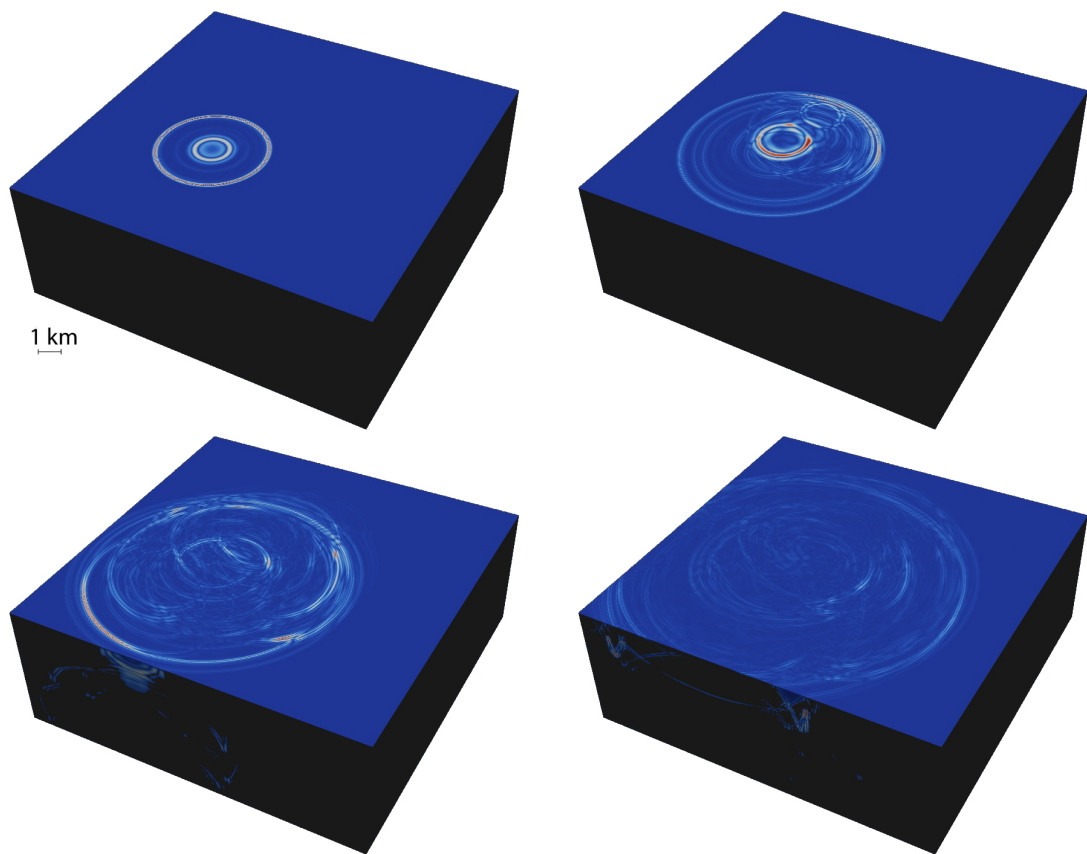


**Figure 9.** Wavefield snapshots for an exploration geophysics simulation taken after 5 s, 10 s, 15 s and 20 s. Plotted are vertical velocities at the free surface of the water layer.

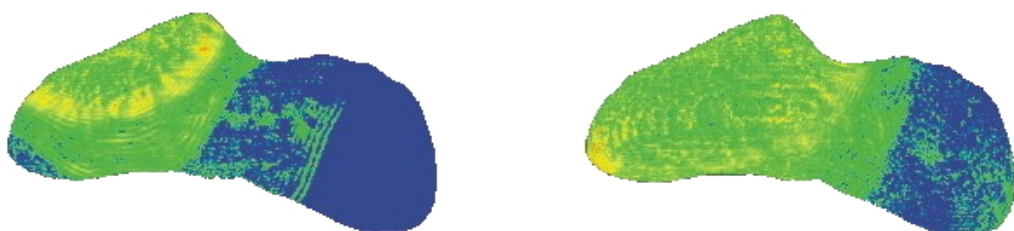
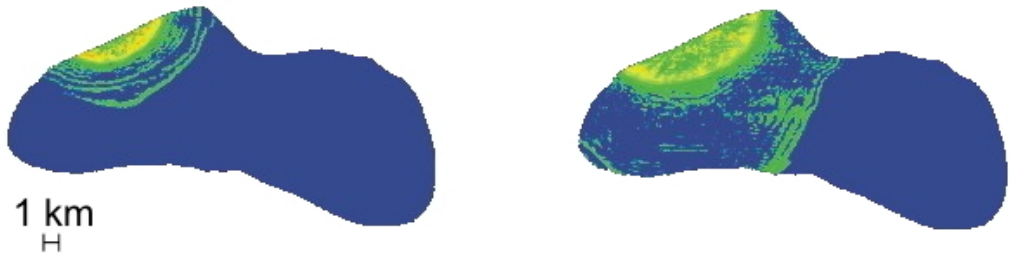


**Figure 10.** Wavefield snapshots for an asteroid simulation taken after 3 s, 4.5 s, 6.5 s and 10.5 s. Plotted is the norm of the velocity at the free surface of the asteroid.

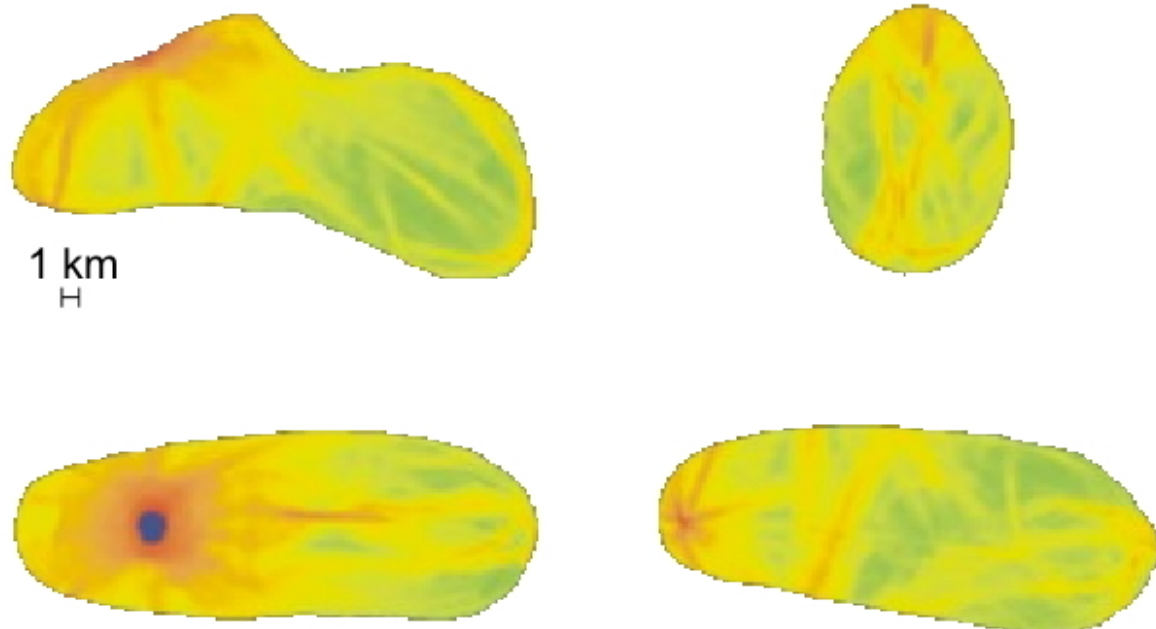


**Figure 11.** ShakeMap views for an asteroid simulation. Plotted are different views of the peak ground accelerations at the free surface of the asteroid.

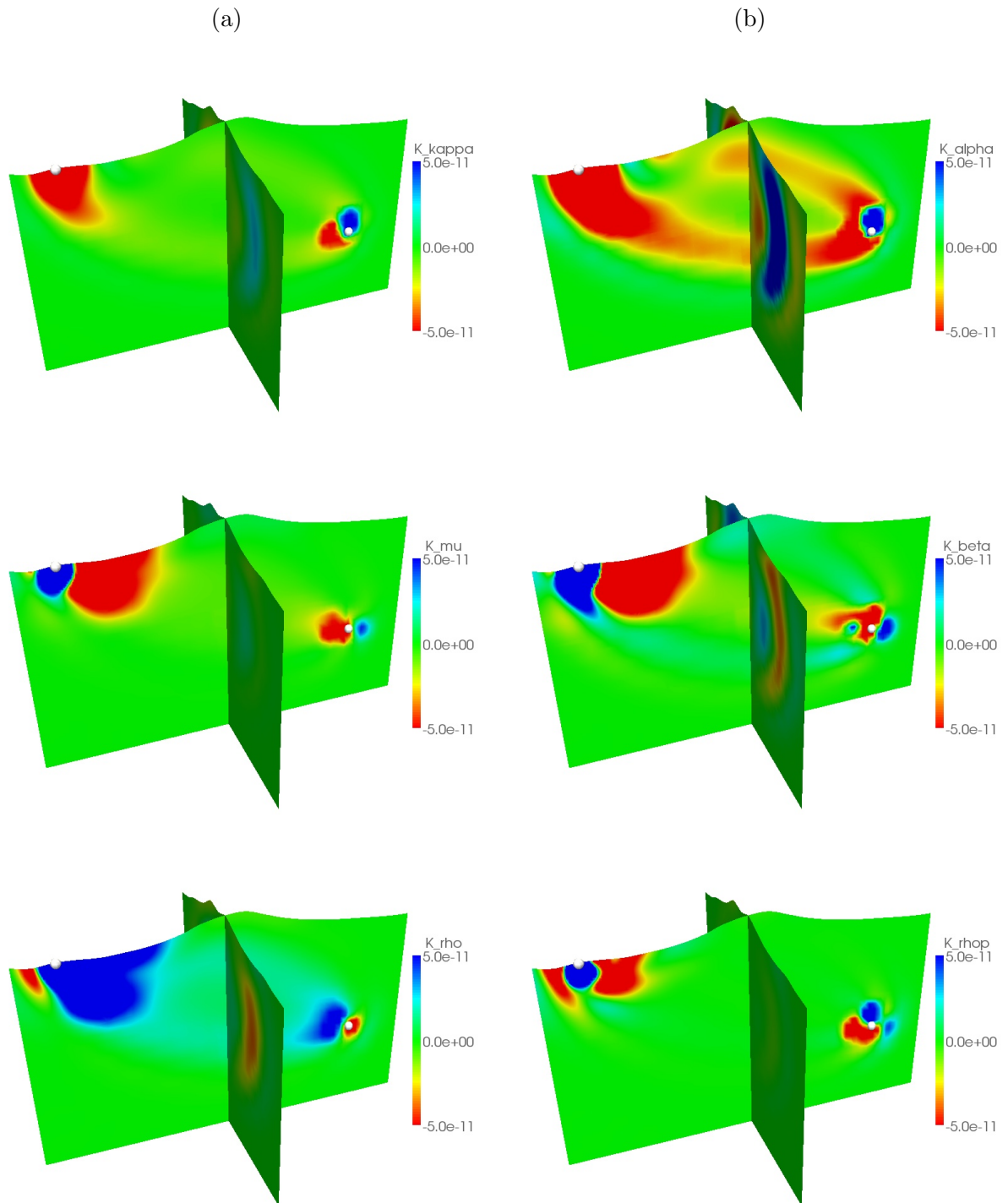


**Figure 12.** Traveltime sensitivity to elastic structure. Fréchet derivatives for isotropic parameterizations (a)  $K_\kappa$ ,  $K_\mu$  &  $K_\rho$  and (b)  $K_\alpha$ ,  $K_\beta$  &  $K'_\rho$  are compared in a model of Mount St. Helens using travelttime adjoint sources for the P wave. Shown are vertical cross sections through the source-receiver line and perpendicular to this line.

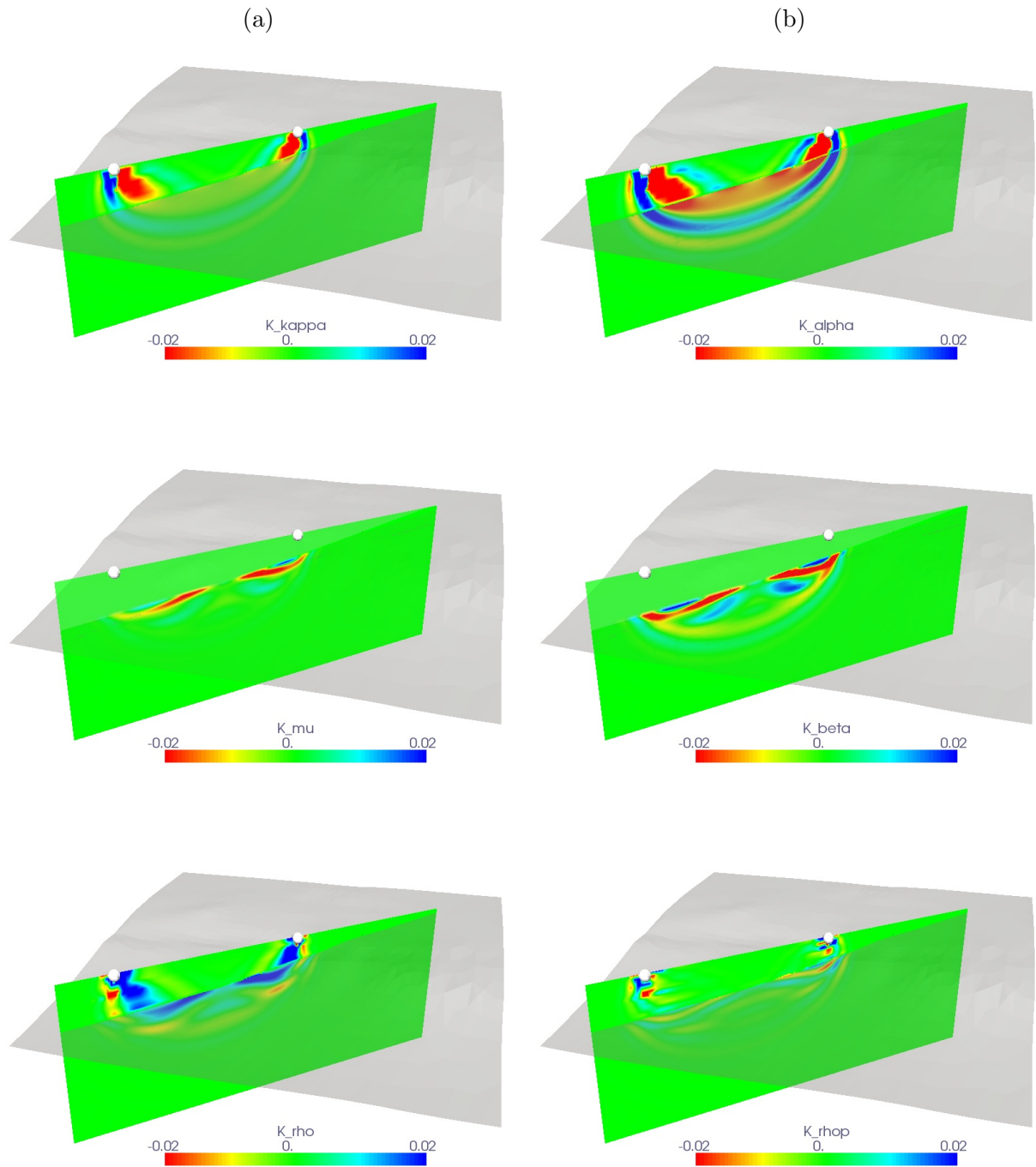


**Figure 13.** Waveform sensitivity to acoustic and elastic structure in a coupled fluid-solid simulation. The bathymetric surface of the Pearl Harbor model, separating the two media, is shown in gray together with a vertical cross-section through source (right) and station (left). Plotted are combined acoustic and elastic kernels using a parameterization (a)  $K_\kappa$ ,  $K_\mu$  &  $K_\rho$  and (b)  $K_\alpha$ ,  $K_\beta$  &  $K'_\rho$ .

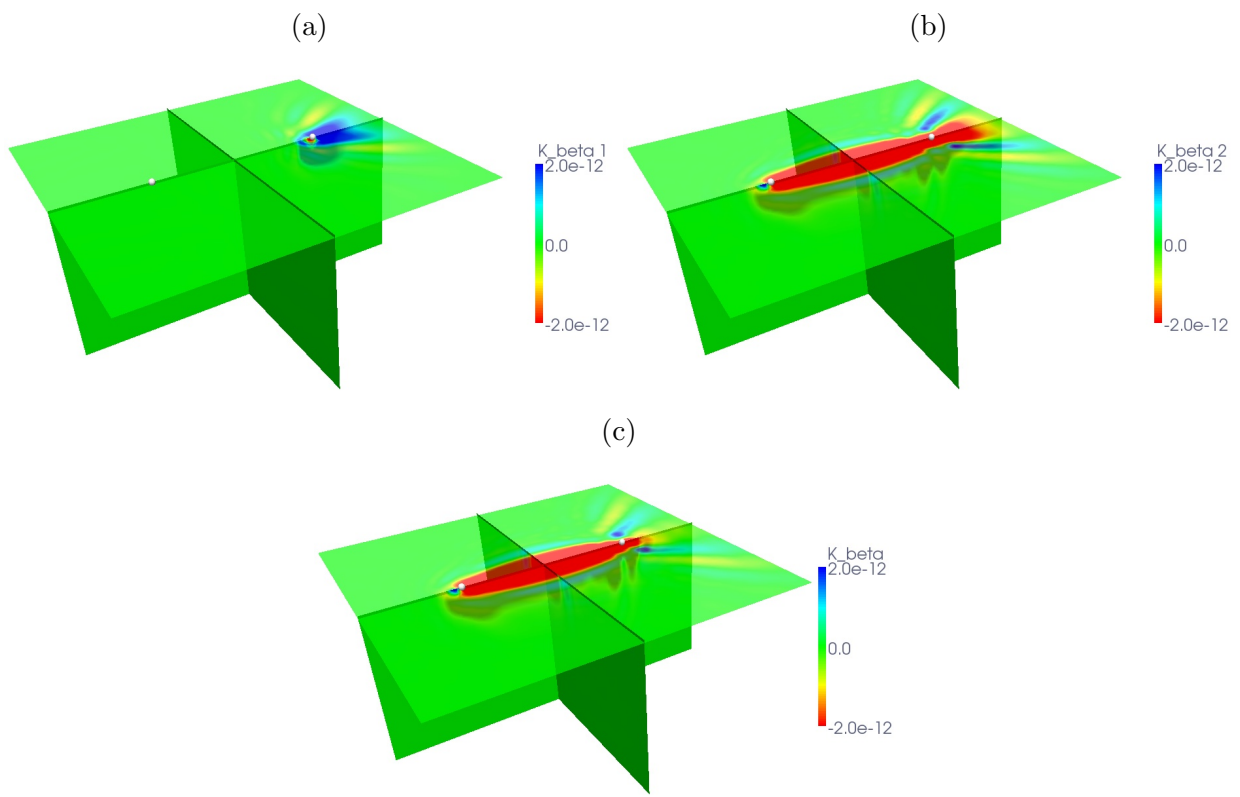


**Figure 14.** Noise cross-correlation sensitivity to elastic structure. Shown are (a) first, (b) second and (c) summed contributions to the  $\langle K_\beta \rangle$  Fréchet derivative in a homogeneous isotropic model. Plotted are vertical and horizontal cross sections through the line connecting the two receivers (white dots) and perpendicular to this line.